



POLITECNICO
MILANO 1863

Automation and Control Engineering

Root Locos
HELICOPTER PROJECT

AUTOMATION AND CONTROL LABORATORY

*Pietro Gualla
Luca Bendazzoli*

supervised by
Prof. Alessandro FALSONE

AY 2022-2023

Abstract

In the following Report several techniques to control a Quanser AERO, a dual-motor setup designed for advanced control research and aerospace applications, will be discussed together with all the necessary steps that led to its control.

In Chapter 1 the System Modelling phase is treated, from the physical description of its non-linear dynamics and its linearization to the estimation of unknown parameters through suitable experiments.

Chapter 2 concerns the Validation of the models derived in Chapter 1 both in Time Domain and Frequency Domain.

Chapter 3 is the core of the Report, it addresses the Control Synthesis and Validation for both the setup's configurations. The first regulator is a SISO Frequency Based Controller for Reference Tracking in the 1 DoF case.

For the 2 DoF configuration, the decoupling of the Pitch and Yaw dynamics is treated together with the design of two SISO Frequency Based Controllers. After this, State Feedback solutions, such as Pole Placement and LQR Control, combined with Luenberger State Observer and Kalman Predictor are discussed for the same control objective. Lastly the possibility of using Model Predictive Control as an advanced approach to achieve Trajectory Tracking is explored.

Key Words: Quanser Aero, Dynamical System Modelling, Friction Estimation, Non-linear System, Coupled System, Mutual Effect Estimation, Aerodynamical Forces, Time Domain Model Validation, Frequency Domain Model Validation, Sine Sweep, PID Control, State Estimation, Luenberger Observer, Kalman Predictor, State Feedback Control, Pole Placement, LQ Control, LQG Control, Model Predictive Control, Reference Tracking, Fixed Attitude Control, Trajectory tracking.

Contents

1 System Modelling	1
1.1 Mathematical Models	2
1.1.1 1 DoF Model	2
1.1.2 2 DoF Model	4
1.2 Model Parameters Identification	8
1.2.1 Friction Coefficients	8
1.2.2 Aerodynamical Forces	11
1.2.3 Mutual Effects	13
1.2.4 COG Position	15
2 Model Validation	16
2.1 1 DoF Model	16
2.1.1 Time Domain Validation	16
2.1.2 Frequency Domain Validation	17
2.2 2 DoF Model	19
2.2.1 Time Domain Validation	19
2.2.2 Frequency Domain Validation	20
3 Control Design and Validation	21
3.1 1DoF Frequency Based Control	21
3.1.1 Synthesis	21
3.1.2 Validation	23
3.2 2DoF Frequency Based Control	25
3.2.1 Synthesis	25
3.2.2 Validation	28
3.3 Pole Placement with State Observer	30
3.3.1 Synthesis	30
3.3.2 Validation	31
3.4 LQG Control	34
3.4.1 Synthesis	34
3.4.2 Validation	35
3.5 Model Predictive Control	37
3.5.1 Synthesis	37
3.5.2 Validation	38
A Explicit Results	1
B Used Simulink Control Schemes	2

Chapter 1

System Modelling



Figure 1.1: VTOL Setup



Figure 1.2: Helicopter Setup

Introduction

The Quanser Aero system is used to simulate the behaviour of multiple flying vehicles, such as VTOLs (Vertical Take-off and Landing), as shown in [Figure 1.1](#) or Half-Quadcopters and Helicopters [Figure 1.2](#).

The possibility of switching the configurations is given by the fact that one of the two thrusters (Motor 1) can be rotated and that the Yaw angle motion can be locked.

VTOL configuration is characterized by the Yaw rotation being locked and by Motor 1 being parallel to Motor 0, from now on this will be addressed as *1 DoF configuration*.

The Half-Quadcopter one still has the Yaw rotation locked but with Motor 1 being perpendicular to Motor 0, this will not be considered in the following report.

Helicopter configuration instead, while having the two motors perpendicular, allows Yaw rotations. In this case the system becomes a 2 DoF one and so this configuration will be addressed as *2 DoF Configuration*.

Analysing the system from an Input/Output perspective, it is clear that its control variables are the voltages supplied to the motors, while its outputs are the Pitch and Yaw angles.

We considered both DC-Motors as ideal actuators (*i.e. infinite bandwidth*) being the electrical dynamics much faster than the mechanical one. Under these assumptions, the thrusters instantaneously convert the supplied voltages into forces applied to the mechanical system. → [Click here to see how](#) ←

For this reason, from now on, only the strictly mechanical dynamics will be modelled with the aim of describing the I/O relationship between the forces applied by the thrusters(F_0 and F_1) and the measured Pitch and Yaw angles(θ and ϕ).

Since not every parameter of the system is known, in [section 1.2](#) the identification of the missing parameters will be treated, note that in [section 1.1](#) they will be considered as given.

1.1 Mathematical Models

Model Parameters

1.1.1 1 DoF Model

In this configuration motions along the Yaw axis are physically locked and the two thrusters are parallel. In [Figure 1.3](#) it is shown the forces and torques balance.

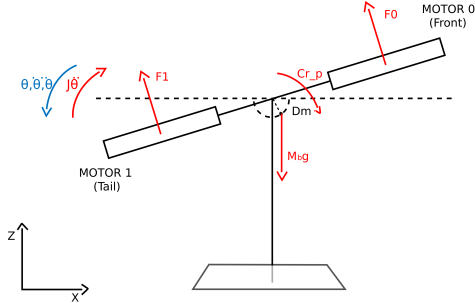


Figure 1.3: 1 DoF system representation

Non-Linear Model

Centering the **reference frame origin** in the Pitch hinge, it is possible to write the [Lagrangian equation](#) as follows:

$$\frac{d}{dt} \left(\frac{\partial T}{\partial \dot{\theta}} \right) - \frac{\partial T}{\partial \theta} + \frac{\partial D}{\partial \dot{\theta}} + \frac{\partial V}{\partial \theta} = Q_f$$

where:

$$T = \frac{1}{2}(J_p + M_b D_m^2) \dot{\theta}^2, \quad D = \frac{1}{2} k_{pitch} \dot{\theta}^2, \quad V = -M_b g D_m \cos \theta$$

By means of computation we obtain the following Dynamic Torque Balance around the Pitch axis:

$$(J_p + M_b D_m^2) \ddot{\theta} + k_{pitch} \dot{\theta} + M_b g D_m \sin \theta = (F_0 - F_1) D_t \quad (1.1)$$

Linearized Model

Once derived the non-linear model, with a view to frequency based control which needs to be designed on a linear model, we computed its linearization.

Thus, given the Taylor Series Expansions of sine and cosine function, we exploited the following equations to linearize the Pitch dynamics described in [Equation 1.1](#):

$$\begin{cases} \cos \tilde{\theta} = \cos \theta_0 - \sin \theta_0 \theta \\ \sin \tilde{\theta} = \sin \theta_0 + \cos \theta_0 \theta \end{cases} \quad (1.2)$$

The linearized 1 DoF model equation results in:

$$(J_p + M_b D_m^2) \ddot{\theta} + k_{pitch} \dot{\theta} + (M_b g D_m \cos \theta_0) \theta = D_t (F_0 - F_1) - M_b g D_m \sin \theta_0 \quad (1.3)$$

Transfer Function Model

Starting from the linearized [Equation 1.3](#) it is possible to compute the Transfer Function from the difference between the forces generated by the two thrusters ($F_0 - F_1$) to the Pitch Angle θ and the Transfer Function between a dummy signal $\sin \theta_0$, related to a linearization static term, to the Pitch angle θ :

$$\Theta(s) = G(s)(F_0 - F_1) + H(s) \sin \theta_0 \quad (1.4)$$

Where:

$$G(s) = \frac{D_t}{(J_{pitch} + M_b D_m^2)s^2 + k_{pitch}s + (M_b g D_m \cos \theta_0)}$$

$$H(s) = \frac{M_b g D_m}{(J_{pitch} + M_b D_m^2)s^2 + k_{pitch}s + (M_b g D_m \cos \theta_0)}$$

Notice that for a linearization around zero ($\theta_0 = 0$), $\sin \theta_0 = 0$ and $\cos \theta_0 = 1$, the linearization 'disturbance' is null.

The following figures have multiple Bode diagrams because we considered the working region between 0° and 45° , since the linearization position changes the complex conjugate poles, we wanted to represent both the extremes to show the differences.

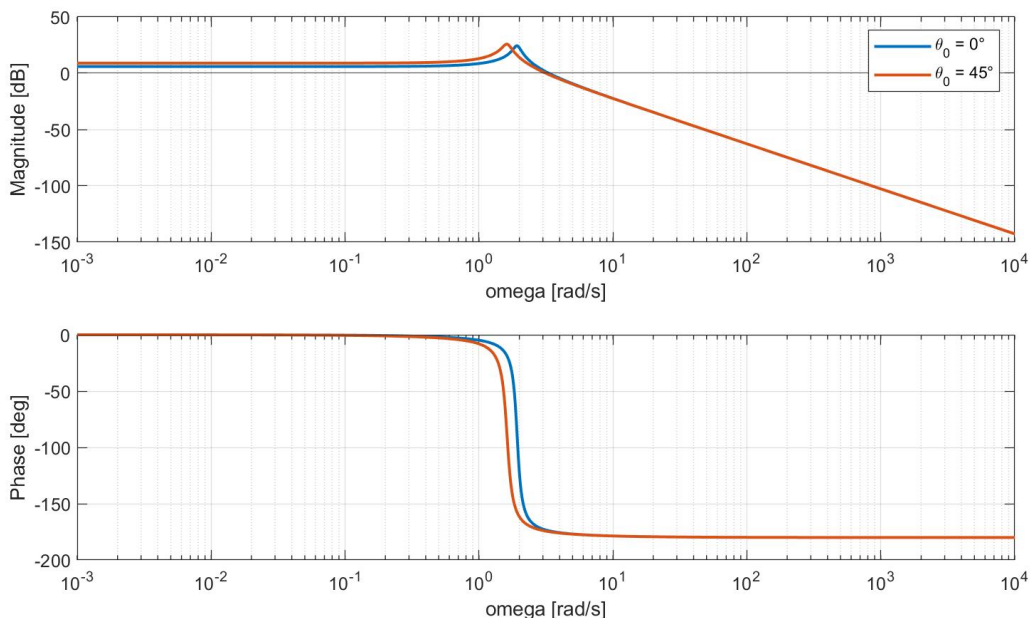
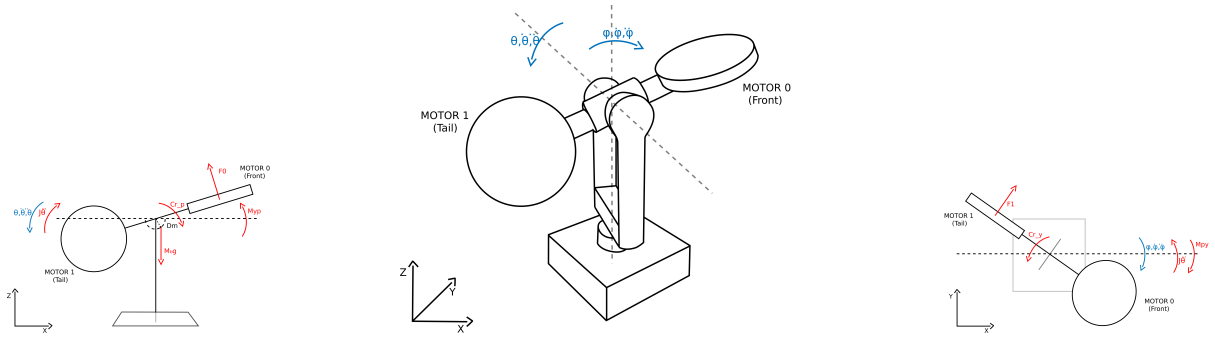


Figure 1.4: $G(s)$ 1 DoF

1.1.2 2 DoF Model



Non-Linear Model

Here are described the equations regarding the coupled dynamics of the system.
The Lagrangian terms are:

$$T = \frac{1}{2}(J_p\dot{\theta}^2 + M_bD_{m2}^2\dot{\theta}^2 + J_y\cos^2\theta\dot{\phi}^2 + M_bD_{m2}^2\sin^2\theta\dot{\phi}^2),$$

$$D = \frac{1}{2}(k_{pitch}\dot{\theta}^2 + k_{yaw}\dot{\phi}^2), \quad V = -M_bgD_{m2}\cos\theta$$

Pitch Dynamics

$$\frac{d}{dt}\left(\frac{\partial T}{\partial \dot{\theta}}\right) - \frac{\partial T}{\partial \theta} + \frac{\partial D}{\partial \dot{\theta}} + \frac{\partial V}{\partial \theta} = Q_\theta$$

$$(J_p + M_bD_{m2}^2)\ddot{\theta} + k_{pitch}\dot{\theta} + 2(M_bD_{m2}^2 - J_y)\dot{\phi}^2\cos\theta\sin\theta + M_bgD_{m2}\sin\theta = (F_0 + k_{yp}F_1)D_t \quad (1.5)$$

Yaw Dynamics

$$\frac{d}{dt}\left(\frac{\partial T}{\partial \dot{\phi}}\right) - \frac{\partial T}{\partial \phi} + \frac{\partial D}{\partial \dot{\phi}} + \frac{\partial V}{\partial \phi} = Q_\phi$$

$$(J_y\cos^2\theta + M_bD_{m2}^2\sin^2\theta)\ddot{\phi} + k_{yaw}\dot{\phi} = (F_1 + k_{py}F_0)D_t \quad (1.6)$$

where $J_y\cos^2\theta$ is the Yaw Inertia, it is a function of the Pitch Angle as we observed this (and felt with our hands) as a non-negligible effect.

Linearized Model

First of all the equilibria positions were studied then we computed a linearization around them:

Pitch equilibrium:

$$\bar{\theta} = \theta_0, \quad \dot{\bar{\theta}} = 0, \quad \ddot{\bar{\theta}} = 0$$

$$M_bgD_{m2}\sin\theta = (F_0 + k_{yp}F_1)D_t$$

Yaw equilibrium:

$$\bar{\phi} = \phi_0, \quad \dot{\bar{\phi}} = 0, \quad \ddot{\bar{\phi}} = 0$$

$$0 = (F_1 + K_{py}F_0)D_t$$

Pitch Dynamics Neglecting the high order parts and considering the equilibrium, the term $2(M_b D_{m2}^2 - J_y) \dot{\phi}^2 \cos \theta \sin \theta$ of the Equation 1.5 comes to zero. $\sin \theta$ and $\cos \theta$ have been linearized with Taylor's expansion seen in Equation 1.2

$$(J_p + M_b D_{m2}^2) \ddot{\theta} + k_{pitch} \dot{\theta} + M_b g D_{m2} (\sin \theta_0 + \cos \theta_0 \theta) = (F_0 + k_{yp} F_1) D_t$$

Results in:

$$(J_p + M_b D_{m2}^2) \ddot{\theta} + k_{pitch} \dot{\theta} + M_b g D_{m2} \cos \theta_0 \theta = (F_0 + k_{yp} F_1) D_t - M_b g D_{m2} \sin \theta_0 \quad (1.7)$$

Yaw Dynamics In Equation 1.6 the only non-linear term is the inertial one. Since this non-linearity is negligible, we linearized the Yaw Dynamics at order zero:

$$(J_y \cos^2 \theta_0 + M_b D_{m2}^2 \sin^2 \theta_0) \ddot{\phi} + k_{yaw} \dot{\phi} = (F_1 + k_{py} F_0) D_t \quad (1.8)$$

State Space Model

Once obtained the previous linearization, the state space model is a direct consequence:

$$\begin{cases} \dot{x} = Ax + Bu \\ y = Cx \end{cases} \quad (1.9)$$

$$\begin{aligned} \begin{bmatrix} \dot{\theta} \\ \ddot{\theta} \\ \dot{\phi} \\ \ddot{\phi} \end{bmatrix} &= \begin{bmatrix} 0 & 1 & 0 & 0 \\ a_{21} & a_{22} & 0 & 0 \\ 0 & 0 & 0 & 1 \\ 0 & 0 & 0 & a_{44} \end{bmatrix} \begin{bmatrix} \theta \\ \dot{\theta} \\ \phi \\ \dot{\phi} \end{bmatrix} + \begin{bmatrix} 0 & 0 \\ b_{21} & b_{22} \\ 0 & 0 \\ b_{41} & b_{42} \end{bmatrix} \begin{bmatrix} F_0 \\ F_1 \end{bmatrix} \\ \begin{bmatrix} \theta \\ \phi \end{bmatrix} &= \begin{bmatrix} 1 & 0 & 0 & 0 \\ 0 & 0 & 1 & 0 \end{bmatrix} \begin{bmatrix} \theta \\ \dot{\theta} \\ \phi \\ \dot{\phi} \end{bmatrix} + \begin{bmatrix} 0 & 0 \\ 0 & 0 \end{bmatrix} \begin{bmatrix} F_0 \\ F_1 \end{bmatrix} \end{aligned}$$

Where:

$$a_{21} = \frac{-M_b g D_{m2} \cos \theta_0}{J_p + M_b D_{m2}^2}, \quad a_{22} = \frac{-k_{pitch}}{J_p + M_b D_{m2}^2}, \quad a_{44} = \frac{-k_{yaw}}{J_y \cos^2 \theta_0 + M_b D_{m2}^2 \sin^2 \theta_0}$$

$$b_{21} = \frac{D_t}{J_p + M_b D_{m2}^2}, \quad b_{22} = \frac{k_{yp} D_t}{J_p + M_b D_{m2}^2}, \quad b_{41} = \frac{D_t}{J_y \cos^2 \theta_0 + M_b D_{m2}^2 \sin^2 \theta_0}, \quad b_{42} = \frac{k_{py} D_t}{J_y \cos^2 \theta_0 + M_b D_{m2}^2 \sin^2 \theta_0},$$

Enlarged State Space Model

The Enlarged System has been used in those control schemes where an integral action of the feedback-error was required.

$$\begin{cases} \dot{\eta}_\theta = \theta_0 - \theta \\ \dot{\eta}_\phi = \phi_0 - \phi \end{cases}$$

Including these new two states, the enlarged system becomes:

$$\begin{cases} \dot{x}_e = A_e x_e + B_e u + M_e y_0 \\ y = C_e x_e \end{cases} \quad (1.10)$$

where:

$$A_e = \begin{bmatrix} A & 0 \\ -C & 0 \end{bmatrix} \quad B_e = \begin{bmatrix} B \\ 0 \end{bmatrix} \quad C_e = [C \ 0] \quad M_e = \begin{bmatrix} 0 \\ I \end{bmatrix}$$

resulting in:

$$\begin{bmatrix} \dot{\theta} \\ \ddot{\theta} \\ \dot{\phi} \\ \ddot{\phi} \\ \dot{\eta}_\theta \\ \dot{\eta}_\phi \end{bmatrix} = \begin{bmatrix} 0 & 1 & 0 & 0 & 0 & 0 \\ a_{21} & a_{22} & 0 & 0 & 0 & 0 \\ 0 & 0 & 0 & 1 & 0 & 0 \\ 0 & 0 & 0 & a_{44} & 0 & 0 \\ -1 & 0 & 0 & 0 & 0 & 0 \\ 0 & 0 & -1 & 0 & 0 & 0 \end{bmatrix} \begin{bmatrix} \theta \\ \dot{\theta} \\ \phi \\ \dot{\phi} \\ e_\theta \\ e_\phi \end{bmatrix} + \begin{bmatrix} 0 & 0 \\ b_{21} & b_{22} \\ 0 & 0 \\ b_{41} & b_{42} \\ 0 & 0 \\ 0 & 0 \end{bmatrix} \begin{bmatrix} F_0 \\ F_1 \end{bmatrix} + \begin{bmatrix} 0 & 0 \\ 0 & 0 \\ 0 & 0 \\ 1 & 0 \\ 0 & 1 \end{bmatrix} \begin{bmatrix} \theta_0 \\ \phi_0 \end{bmatrix}$$

$$\begin{bmatrix} \theta \\ \phi \end{bmatrix} = \begin{bmatrix} 1 & 0 & 0 & 0 & 0 & 0 \\ 0 & 0 & 1 & 0 & 0 & 0 \end{bmatrix} \begin{bmatrix} \theta \\ \dot{\theta} \\ \phi \\ \dot{\phi} \\ e_\theta \\ e_\phi \end{bmatrix}$$

Where:

$$a_{21} = \frac{-M_b g D m^2 \cos \theta_0}{J_p + M_b D_{m2}^2}, \quad a_{22} = \frac{-k_{pitch}}{J_p + M_b D_{m2}^2}, \quad a_{44} = \frac{-k_{yaw}}{J_y \cos \theta_0^2 + M_b D_{m2}^2 \sin \theta_0^2}$$

$$b_{21} = \frac{D_t}{J_p + M_b D_{m2}^2}, \quad b_{22} = \frac{k_{yp} D_t}{J_p + M_b D_{m2}^2}, \quad b_{41} = \frac{D_t}{J_y \cos \theta_0^2 + M_b D_{m2}^2 \sin \theta_0^2}, \quad b_{42} = \frac{k_{py} D_t}{J_y \cos \theta_0^2 + M_b D_{m2}^2 \sin \theta_0^2},$$

State Space Model with Stochastic Noises

The State-Space Model reported has been used in those control schemes in which, for assumption, the process is affected by stochastic noises. More precisely, there is an additive white noise on the state $v_x \sim WN(0, \tilde{Q})$ and another one on the output $v_y \sim WN(0, \tilde{R})$.

$$\begin{cases} \dot{x} = Ax + Bu + v_x(t) \\ y = Cx + v_y(t) \end{cases} \quad (1.11)$$

These noises model, through their covariance matrices, respectively how much the Model and the Sensor are trustworthy.

Transfer Function Models

The transfer functions of the 2 DoF dynamics will be used for the Regulators synthesis

$$\begin{bmatrix} \Theta(s) \\ \Phi(s) \end{bmatrix} = \begin{bmatrix} G_{11}(s) & G_{12}(s) \\ G_{21}(s) & G_{22}(s) \end{bmatrix} \begin{bmatrix} F_0 \\ F_1 \end{bmatrix} + \begin{bmatrix} H_1 \\ 0 \end{bmatrix} [\sin \theta_0] \quad (1.12)$$

where:

$$G_{11}(s) = \frac{D_t}{(J_p + M_b D_{m2}^2)s^2 + k_{pitch}s + M_b g D_{m2} \cos \theta_0} \quad (1.13)$$

$$G_{12}(s) = \frac{k_{yp} D_t}{(J_p + M_b D_{m2}^2)s^2 + k_{pitch}s + M_b g D_{m2} \cos \theta_0} \quad (1.14)$$

$$G_{22}(s) = \frac{D_t}{(J_y \cos^2 \theta_0 + M_b D_{m2}^2 \sin^2 \theta_0)s^2 + k_{yaw}s} \quad (1.15)$$

$$G_{21}(s) = \frac{k_{py} D_t}{(J_y \cos^2 \theta_0 + M_b D_{m2}^2 \sin^2 \theta_0)s^2 + k_{yaw}s} \quad (1.16)$$

$$H_1(s) = \frac{M_b g D_{m2}}{(J_p + M_b D_{m2}^2)s^2 + k_{pitch}s + M_b g D_{m2} \cos \theta_0} \quad (1.17)$$

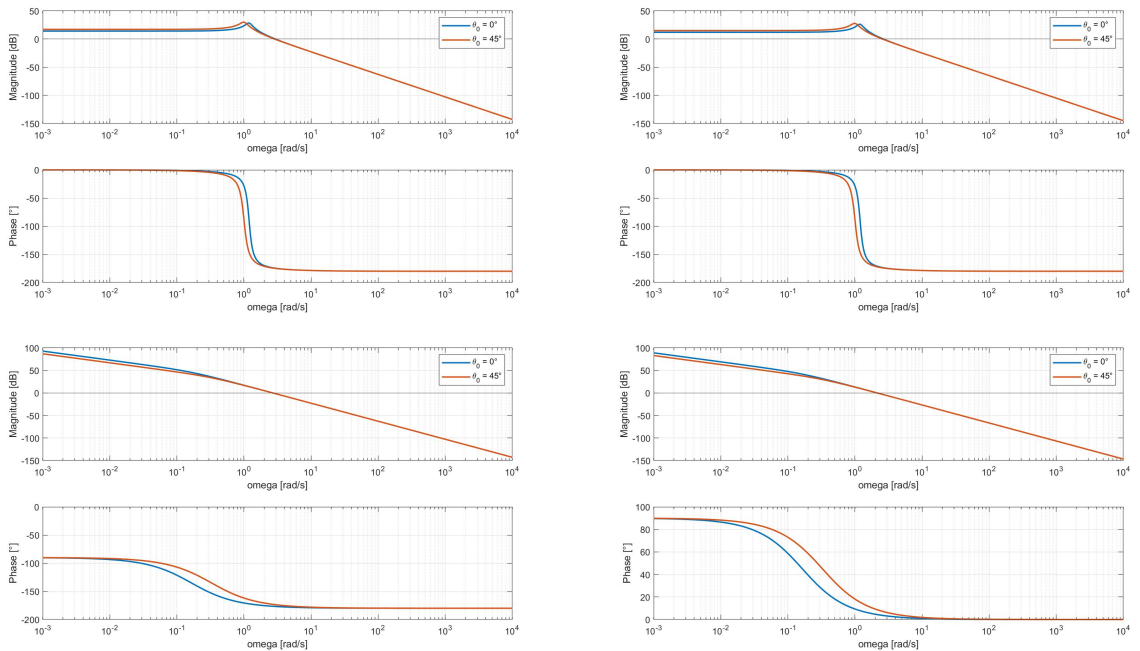


Figure 1.6: 2DoF Transfer Functions $G_{11}(s), G_{12}(s), G_{21}(s), G_{22}(s)$

1.2 Model Parameters Identification

1.2.1 Friction Coefficients

Experiments Overview

The Pitch friction estimation was made in *1 DoF Configuration* in order to isolate the studied behaviour and with the Motors off, to reduce at best the uncertainty sources (also because we didn't have the Motor Maps yet).

For completeness we also realised some experiments forcing the system with the Motors. To estimate the Yaw friction, similarly to the previous experiment, we locked the Pitch movement while in *2 DoF Configuration*.

In this case a "decaying step" reference ($18V \rightarrow 0V$) was supplied to Motor 1 in order to analyze how friction acted on the Yaw Dynamics counteracting kinetic energy and leading the setup to stop.

Pitch Friction Coefficient k_{pitch}

In the first place, we manually forced the system by letting it oscillate realising it from its maximum Pitch angle and observed a damped oscillation. Since the Pitch Dynamics can be seen as a real pendulum, the first idea was to use a second order homogeneous differential equation to describe the damped periodic behaviour of the physical model:

$$y(t) = Ae^{-\alpha t} \cos(\omega_d t + \varphi) \quad (1.18)$$

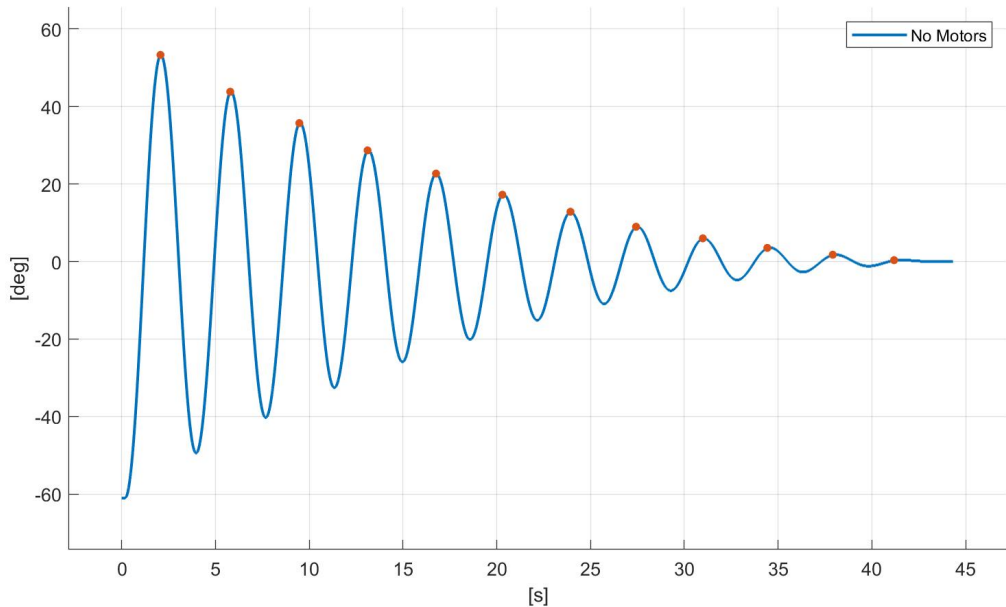


Figure 1.7: Motors OFF

Once obtained the acquisition, we decided to fit it through Least Mean Square algorithm with the theoretical damped [Equation 1.18](#) to learn the value of α which then would have allowed us to compute k_{pitch} as: $k_{pitch} = -2\alpha(J_p + M_b D_m^2)$.

Since the fitting was not satisfactory, especially with small angles, we decided to divide

the experiment in two parts, the first one between the start and 20° degrees angle and the second from 20° to the end of the acquisition.

By averaging the two found solutions, we obtained:

$$k_{pitch}^{n1} = 0.0052 \frac{Nm}{(rad/s)}$$

Once identified it in this way, we proceeded with the forced experiments. Similarly to the previous situation, all peaks of the response were found.

This time the mathematical solution was different, the desired coefficient was found using the decrement ratio and the critical damping of the system.

This approach regards a typical response of a second order under-damped system:

$$k_{pitch} = 2\xi\omega_{nat}(J_p + M_bD_m^2) \quad (1.19)$$

Where:

$$\xi = \frac{1}{\sqrt{1+(\frac{2\pi}{\delta})^2}}, \quad \delta = \frac{1}{N} \ln \left(\frac{p_1}{p_N} \right), \quad \omega_{nat} = \frac{\omega_d}{\sqrt{1-\xi^2}}, \quad \omega_d = \frac{2\pi}{T_{osc}}$$

In Figure 1.8 are represented some different responses, the idea was to take more than one experiment in order to take the average of multiple measurements. The overall result is:

$$k_{pitch}^{n2} = 0.0031 \frac{Nm}{(rad/s)}$$

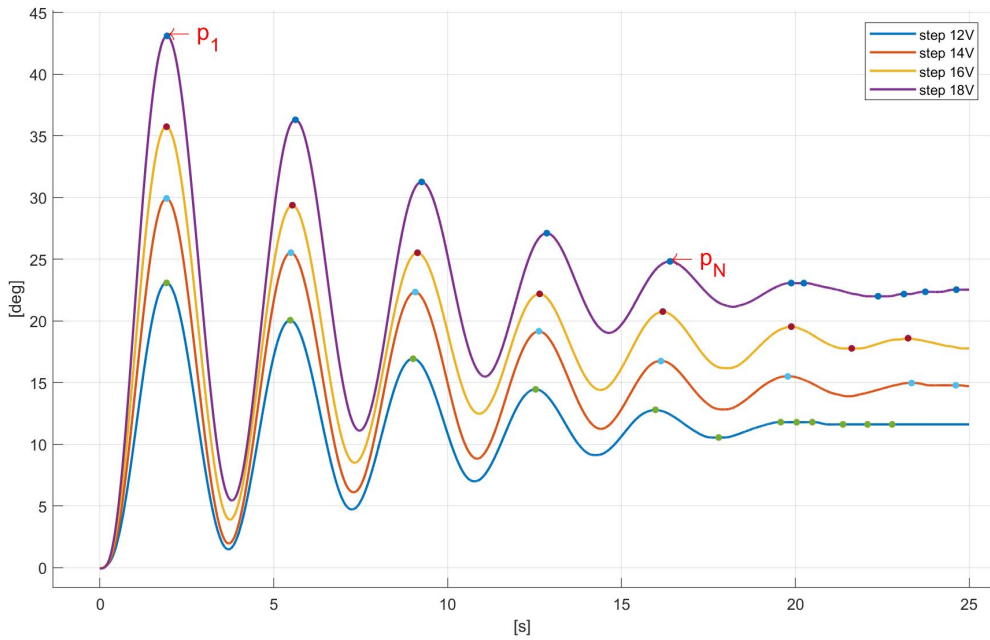


Figure 1.8: Different applied voltage steps

As seen, two results were found. Since the Helicopter manoeuvres are made with motors the second solution was preferable.

Another point that enforces the earlier reasoning is that it is better to under-estimate the friction coefficient because it leads to a more robust Controllers Design, furthermore a more damped system than expected will help the stability.

Yaw Friction Coefficient k_{yaw}

For the Yaw Friction, as previously explained, we exploited a different kind of experiment with respect to k_{pitch} one. The principle of this approach regards the first-order transfer function response.

Analyzing $G_{22}(s)$ in [Equation 1.15](#) it is possible to see how the system has an embedded integral action and so the Yaw dynamics from Force F_1 to Velocity $\dot{\phi}$ can be described with the following first order transfer function:

$$\dot{\Phi}(s) = \frac{(J_y \cos^2 \theta_0 + M_b D_{m2}^2 \sin^2 \theta_0)}{(J_y \cos^2 \theta_0 + M_b D_{m2}^2 \sin^2 \theta_0)s + k_{yaw}} F_1$$

In this way, studying the inverse step response, the friction coefficient can be found as:

$$k_{yaw} = \frac{(J_y \cos^2 \theta_0 + M_b D_{m2}^2 \sin^2 \theta_0)}{\tau} \quad \text{where} \quad \tau = \frac{t_2 - t_0}{5}$$

The setup starts with a constant velocity which decreases until it stops. The time constant τ corresponds to the time taken by the system, after the inverse step reference, to reach the 37% of its final value. To ensure a great result 5τ has been taken into account so the model had to reach the 99.5% of its final value as represented in [Figure 1.9](#).

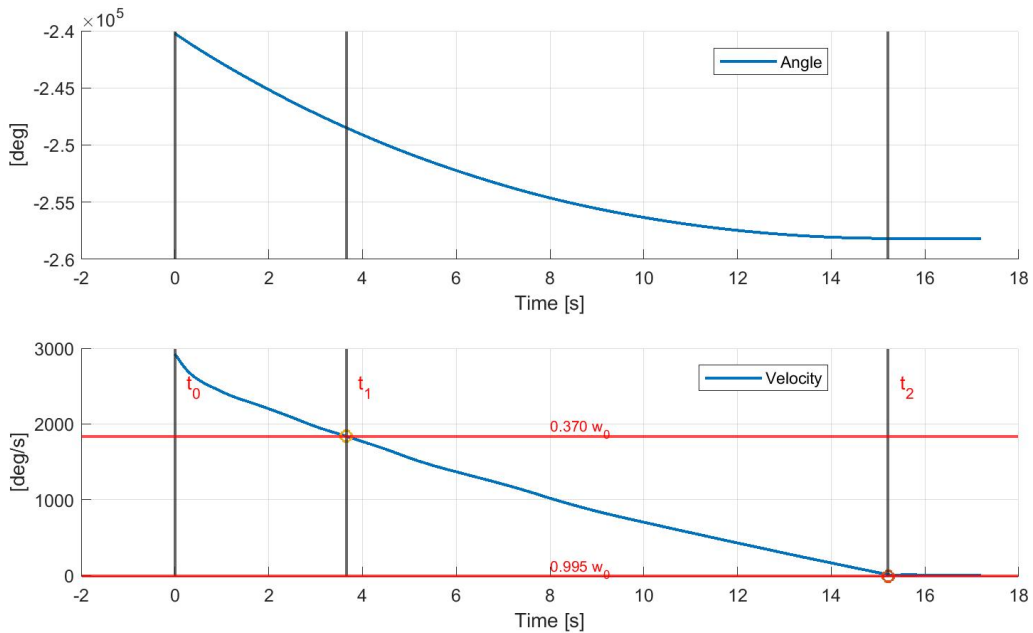


Figure 1.9: Response to Decaying voltage step Analysis

All these considerations led to the following result:

$$k_{yaw} = 0.0039 \frac{Nm}{(rad/s)}$$

1.2.2 Aerodynamical Forces

Experiments Overview

To model the thrusters, we considered the DC motors as ideal actuators (*i.e.: with infinite bandwidth*) neglecting their dynamic behaviour. By means of this simplification, we reduced the motors' operating regions to a steady-state one.

We then designed an experiment to identify the mathematical function relating the voltage V supplied to the motor to the generated thrust force F_{thrust} .

The experiment consists in setting the motors to different voltages and then measure the related equilibrium position at which the setup stabilizes. For each equilibrium position the torque applied by the motor is equal to the opposite of the torque given by the setup's CoG so it is possible to compute the "stabilizing force" at each pitch angle θ through a simple static torque balance.

Motor Direct Map

Our aim was to identify a function describing the relationship between the voltage V and the thrust force F_{thrust} .

Starting from the torque balance around the pitch axis:

$$F_{thrust} D_t = M_b g D_m \sin \theta_{eq} \quad (1.20)$$

we derived:

$$F_{thrust} = \frac{M_b g D_m \sin \theta_{eq}}{D_t} = k_{force} \sin \theta_{eq}$$

We then supplied the setup with several voltages in its working range [-18; 18] [V] and measured the equilibrium pitch angle θ_{eq} associated to that voltage which, through the equation above, allowed us to compute F_{thrust} .

From the experimental data we fitted through a Least Squares Algorithm the Direct Motor Map with a third order polynomial:

$$F_{thrust} = f(V) = w_1 V^3 + w_2 V^2 + w_3 V \quad (1.21)$$

Note that it was necessary to compute four different maps, two for each motor, one for positive and one for negative supplied voltages. This became necessary as the motors does not generate the same thrust in negative and positive direction and, moreover, we discovered that Motor 1 is more powerful than Motor 0 by a 10-15% factor making it impossible to model them with the same map.

We tried to explain this differences coming to the conclusions that Motor 0 is more worn than Motor 1, causing a performance loss. As for the differences related to the sign of the supplied voltage we blame the shape and the position of the electric motors that, in our opinion, could be affecting the performance by interfering with the entering air flow. Moreover we determined that the motors, when subject to positive voltages, also took advantage of some ground effect: the superimposition of these two effects leads to the observed gap. In order to enhance the quality (and the quantity) of the experimental data, during the actual testing on the setup, we supplied the motors with a very slow ramp (0.15V/s slope) which can be considered quasi-static. This new signal did not affect the initial static assumption and gave us the opportunity to obtain almost 70'000 experimental points making our Motor Map estimate much more precise. In the following pages it is shown the comparison between the measured data and the learnt polynomial functions that describe the motor's behaviour.

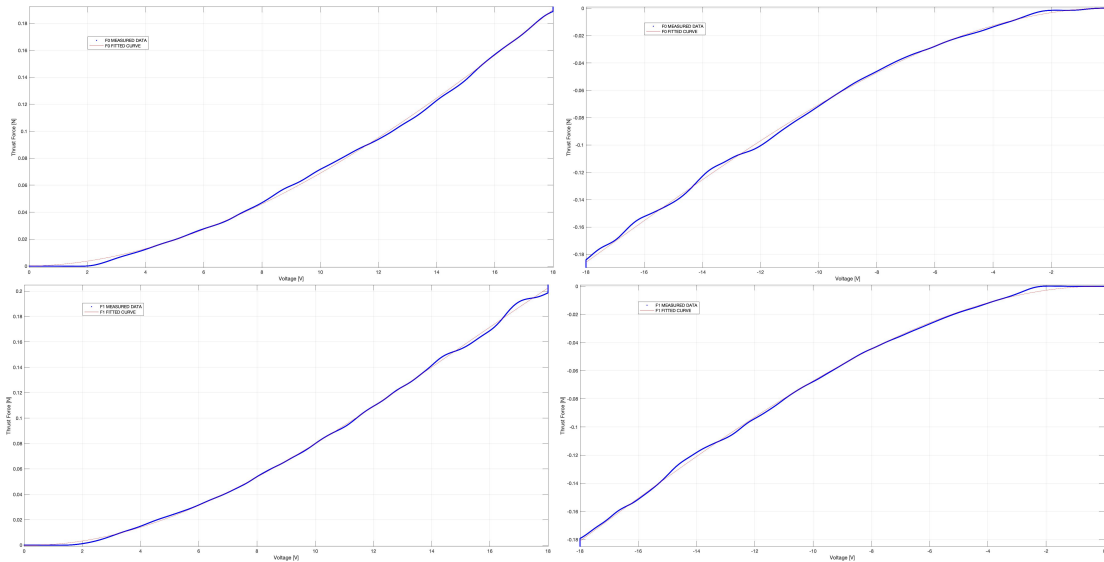


Figure 1.10: F_0^{pos} , F_0^{neg} , F_1^{pos} , F_1^{neg}

Motor Inverse Map

Starting from the ramp experiment previously described we computed the Inverse Maps for the motors.

The Inverse Maps describe the relationship between Force and Voltage, through it one can compute the needed voltage in order to deliver a prescribed force. Being the Motor Direct Map a third order polynomial its inverse function is of difficult computation so we decided to define it by means of a look-up table. From the Direct Map we computed a point-wise relationship between voltage and force and then we inverted it.

1.2.3 Mutual Effects

Experiments Overview

To found the mutual coefficients of the system, we made 4 different experiments. The first two experiments were made with the Pitch locked, while the last two were made with the Yaw locked. The idea was to supplied one Motor at time with a positive ramp voltage reference to slowly increase the provided power.

Pitch to Yaw Mutual Effect k_{py}

To derive the mutual effect coefficient between Motor 0 thrust force F_0 and the Yaw Angle ϕ , we put the setup in locked Pitch configuration and then developed two separate tests. The core idea behind this experiments was to firstly supply Motor 1 (the Direct Motor) with a slow ramp and exploit it to measure the Torque (and indirectly the thrust force F_1) needed on the Yaw Angle in order to make the Helicopter move. We considered the setup in motion after a 2° displacement. Then, we measured the thrust force F_0 delivered by Motor 0 (the Mutual Effect) that made the setup start rotating. The mutual effect coefficient was found as the ratio of these two forces.

Observing the end of the experiment in [Figure 1.11](#), the final Yaw direct angle is more or less twice than the mutual Yaw angle, moreover it is possible to conclude that a positive Voltage on Motor 0 generates a negative motion on the Yaw axis.

The identified mutual effect is:

$$k_{py} = \frac{F_1(\phi = 2^\circ)}{F_0(\phi = 2^\circ)} = -0.64$$

The vertical lines highlight the instants in which the Yaw angle reaches the threshold.

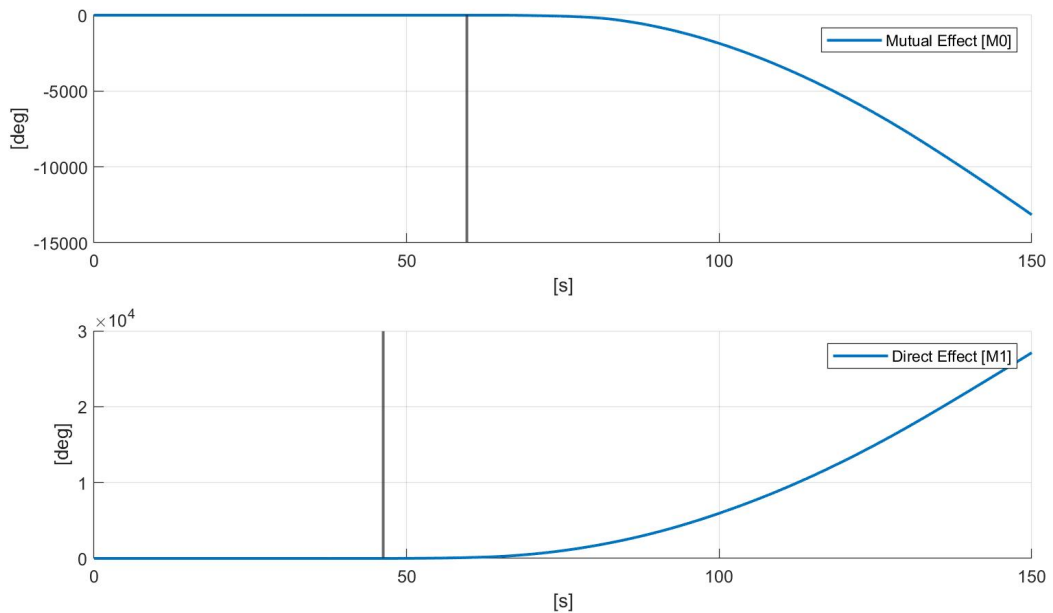


Figure 1.11: Comparison between Direct and Indirect effects

Yaw to Pitch Mutual Effect k_{yp}

The idea behind this identification is the same as the previous one, with the only difference that, in this case, we locked the Yaw Angle.

This time the threshold was set to 1° since the Pitch movement has also the gravitational force that helps to keep the equilibrium of the entire system and the movement was more stable.

From Figure 1.12 it is possible to conclude that, in this case, a positive Voltage on Motor 1 leads to positive movement on the Pitch axis. Moreover it is clear that k_{yp} will be almost unitary since there is no big difference between Direct and Mutual Effect. Again, the vertical lines show the instants in which each Pitch angle reaches the 1° threshold.

The mutual effect has been obtained as:

$$k_{yp} = \frac{F_0(\theta = 1^\circ)}{F_1(\theta = 1^\circ)} = 0.78$$

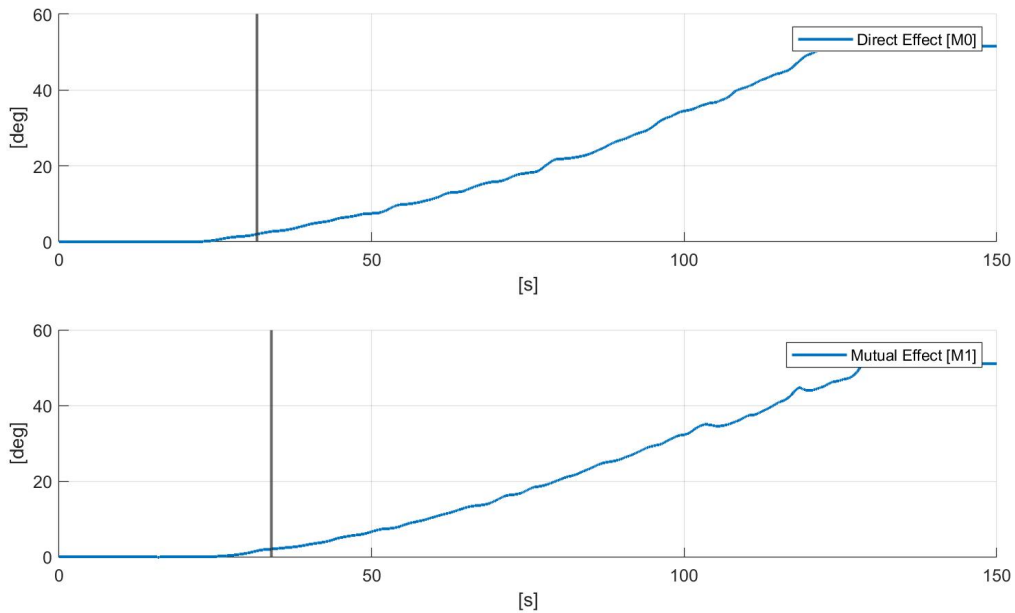


Figure 1.12: Comparison between Direct and Indirect effects

1.2.4 COG Position

Experiments Overview

By analyzing the behaviour of the setup we clearly identified a difference in the CoG position depending on the configuration it was put.

The intuition is a consequence of the observation of the setup dynamics, indeed supplying Motor 0 with a 18V step in *1 DoF configuration* leads to a Pitch response that stabilizes at a pitch angle of 22° , the same input supplied to the *2 DoF configuration* generates a pitch response with a 51° amplitude. The position of the CoG given in the parameters as D_m is actually the one for the *2 DoF configuration*.

Awfully, we discovered this detail far ahead into the modelling phase and, since we had been unwittingly using D_m in the *1 DoF configuration* up to then, we decided to preserve the consistency of the work we had already done and to identify a new *fictitious* parameter D_{m2} for the *2 DoF configuration*.

In the following the experiment for the identification of the new CoG position is discussed.

Position of the CoG D_{m2}

Starting from the torque balance around the Pitch axis [Equation 1.20](#) one obtains that the new parameter to be identified D_{m2} is:

$$D_{m2} = \frac{F_{thrust} D_t}{M_b g \sin \theta_{eq}} = -0.0029 \text{ m}$$

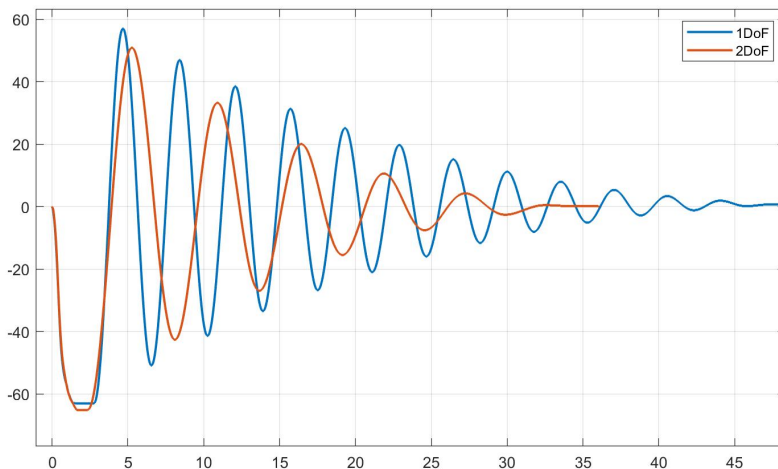


Figure 1.13: Comparison between 1DoF-2DoF Pendulum oscillations

It is obvious that the frequency of oscillation $\omega_{nat} = \sqrt{\frac{M_b D_m \cos \theta_0}{J_p + M_b D_m^2}}$ is different in the two cases. The reason of this change can be attributed only to the CoG position, since the other parameters cannot change.

Chapter 2

Model Validation

2.1 1 DoF Model

2.1.1 Time Domain Validation

In order to validate our model in time domain, we supplied a multi step reference Voltage to cover the entire functioning range and compared the the setup's response to the model's one, in [Figure 2.1](#) it shown the comparison.

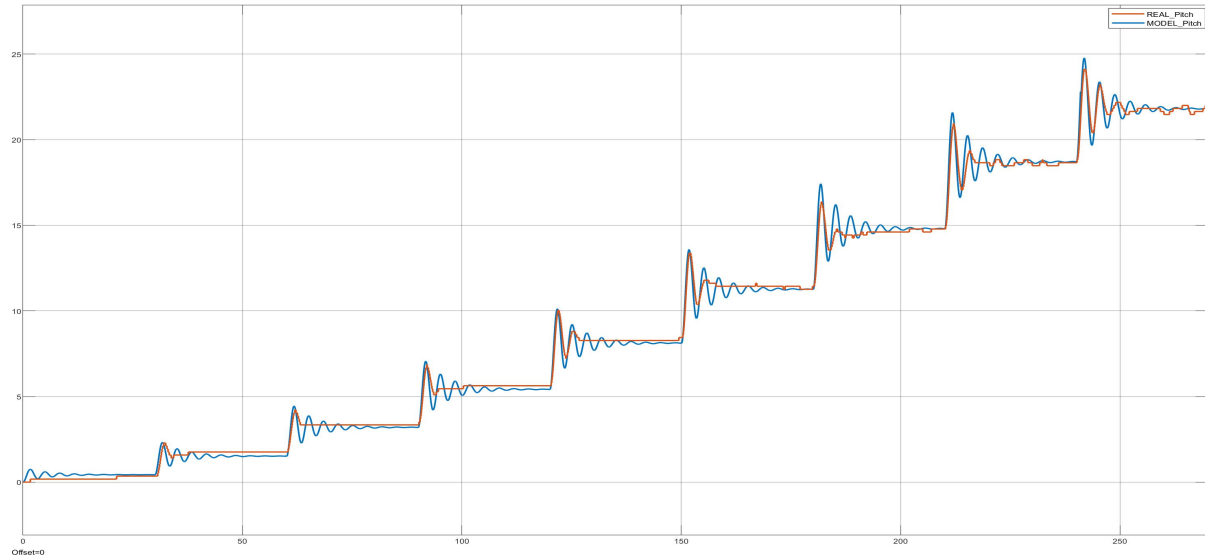


Figure 2.1: 1 DoF Model validation

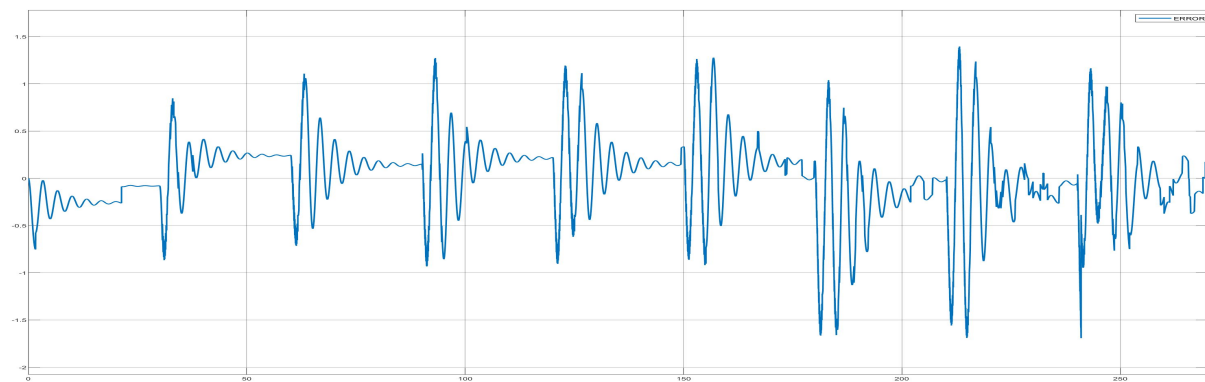


Figure 2.2: 1 DoF Model validation error

Analyzing the figures above the error between the model and the real setup suggest that the friction coefficient is slightly underestimated since the Model' settling time is larger than the Real one, this underestimation is not harmful in terms of control design because shaping a regulator on this model would lead to a more robust control. The steady state error between the two acquisition is quite small, this means that the obtained maps are reliable.

The overall simulation says that the magnitude of the error never exceeds 1.7° in Pitch movements (and does so as a side-effect of damping underestimation).

2.1.2 Frequency Domain Validation

Experiment Overview

In order to validate our model in frequency domain we designed a pseudo-sinesweep experiment to compute in a Black-box fashion the setup's Frequency Response.

The choice of this particular experiment is a consequence of our need to achieve multiple experimental results simultaneously as the building time for code on the setup would have taken itself much more time than the actual experiment, especially for the lower frequencies ones.

A common sinesweep experiment consists in supplying a dynamical system with constant amplitude and increasing frequency sine wave as Input. Analyzing the system's response, it is then possible to infer its Amplitude and Phase Shift with respect to the Input signal at each frequency in order to compute the I/O Bode Diagram.

In our case this kind of approach would have been too heavy from the computational point of view as we would have had to separate very precisely the spectrum components belonging to the frequency of interest from the ones belonging to previous (and still persisting) oscillations.

For this reason in our Input Signal, before each frequency increase, there is a 10 seconds pause. This allowed us during the experiment to realign by hand the Pitch angle in its equilibrium position drastically reducing the effect explained above.

In [Figure 2.3](#) the entire pseudo-sinesweep experiment is shown.

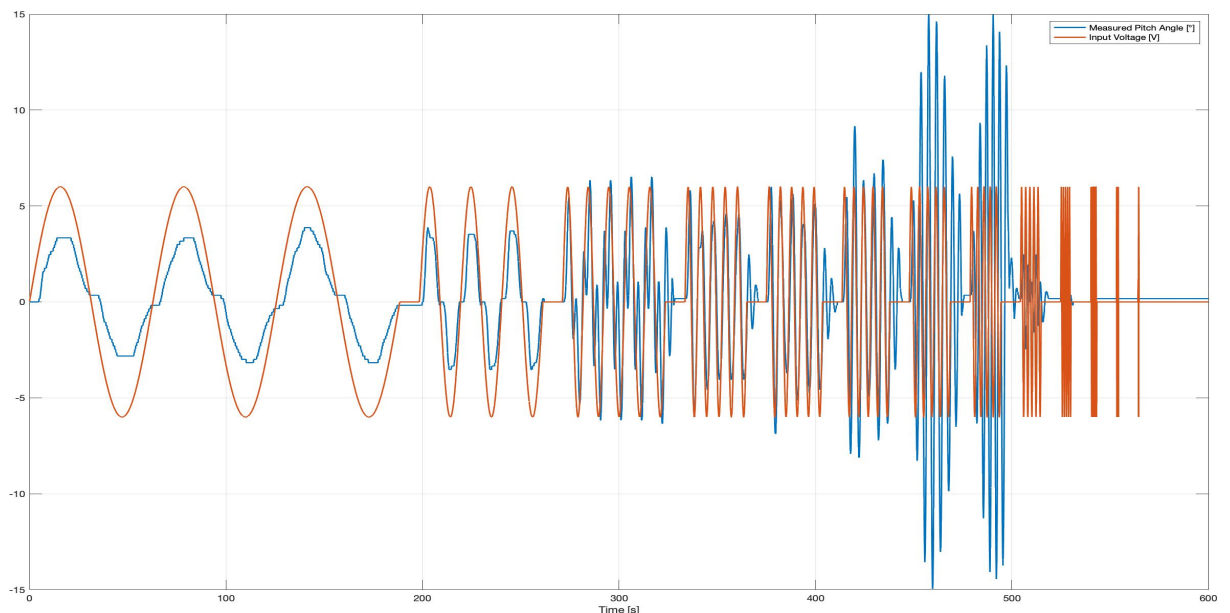


Figure 2.3: Sine Sweep Experiment

Frequency Response Estimation

Once done the experiment, we had to compute both Amplitude and Phase Shift of the setup's Frequency Response from measured data in order to obtain a Bode Plot describing our Helicopter and comparable with our model's one. Since the model we developed in [Equation 1.1](#) describes only the relationship forces to Pitch we made this same experiment on the model enhanced with the Motor Maps found in [subsection 1.2.2](#), in order to achieve a sensate comparison.

Magnitude First of all we calculated the Fourier Transform of both Input and Output Signal, for each frequency of the experiment, then, from the obtained frequency spectrum, the Amplitude was computed as the ratio between Output and Input at each frequency as:

$$|G_{exp}(j\omega^*)| = \frac{\Theta(j\omega^*)}{U(j\omega^*)} \quad (2.1)$$

In [Figure 3.7](#) an example of the FFT output at a given frequency where it is possible to appreciate how the signals' spectra are not punctually located in the perturbation frequency especially on the Output, this also shows the importance of computing the Magnitude in this way. Indeed, by simply dividing the two signals (as we did in the first place) one would get a quite big error due to the superimposition of effects at frequencies other than the one of interest.

Phase Shift The Phase Shift computation was done starting from the Time Domain response to our pseudo-sinesweep and measuring the delay Δt of the Output with respect to the Input signal, as shown in [Figure 3.8](#).

Knowing the Input Signal frequency ω^* it was then possible to obtain the phase shift as follows:

$$\Delta\varphi_{deg} = \frac{180}{pi} \omega^* \Delta t \quad (2.2)$$

Bode Diagram The Amplitude and Phase Shift of the Setup Frequency Response from experimental data are here compared with our model's ones in order to complete the Model Validation. In [Figure 2.4](#) our model's Frequency Domain Validation.

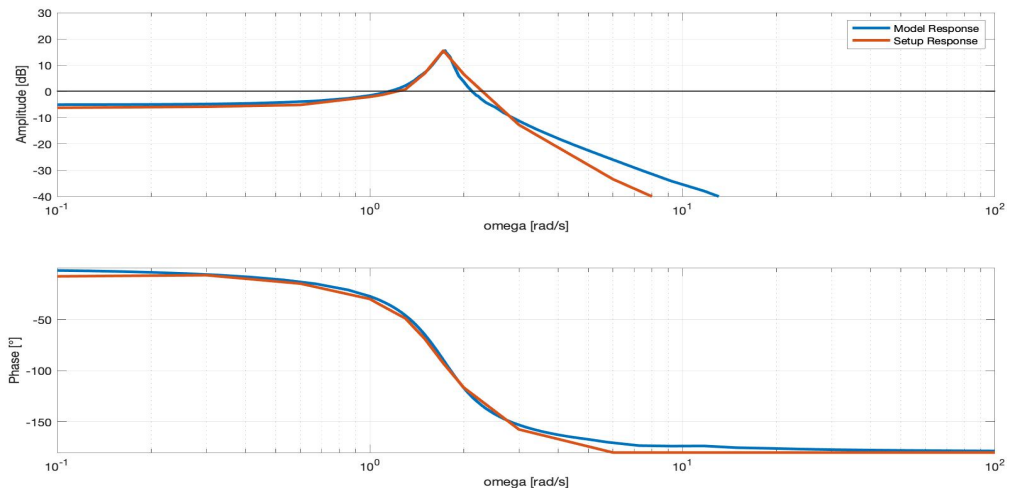


Figure 2.4: Comparison between Setup's and Model's Frequency Responses

2.2 2 DoF Model

2.2.1 Time Domain Validation

For this Model Validation we decided firstly to supply one Motor at the time with a ramp in order to validate the Direct and Mutual Effects. In [Figure 2.5](#) it is shown, by way of example, the case where Motor 1 was supplied. Analyzing [Figure 2.5](#), we can state that the Mutual Effect k_{yp} together with the CoG position D_{m2} were identified correctly since the model tracks almost perfectly the real behaviour.

Once the first mutual effect has been validated, the second one was validated together with k_{yaw} through the dual experiment.

Finally in [Figure 2.6](#) the experiment with both Motor active together (subject to the same ramp signal) is shown, all the plots show that also the 2 DoF Model describes in a good way the setup's behaviours.

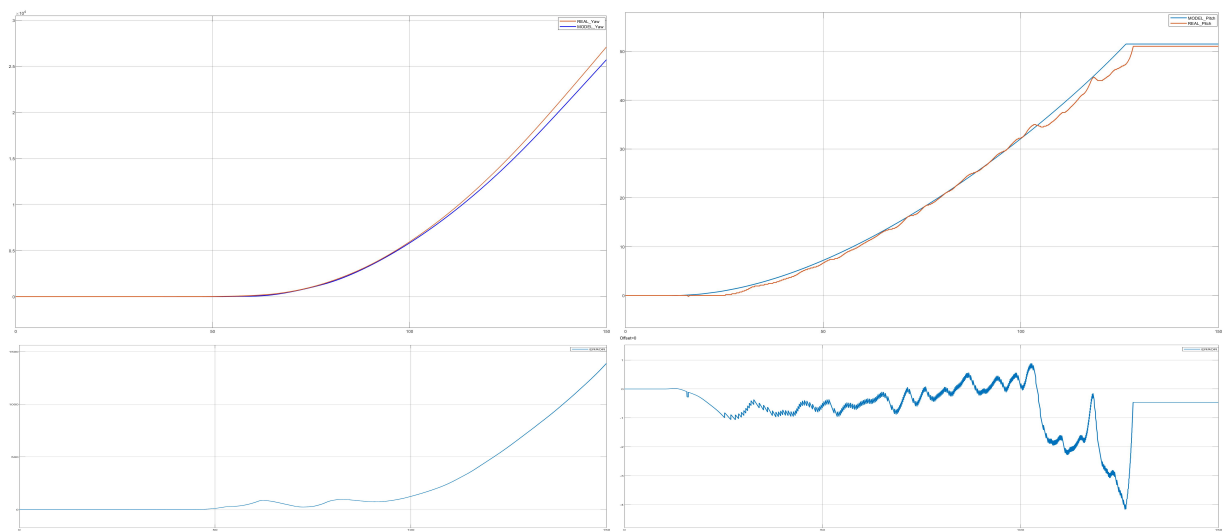


Figure 2.5: Response to Motor 1 Ramp

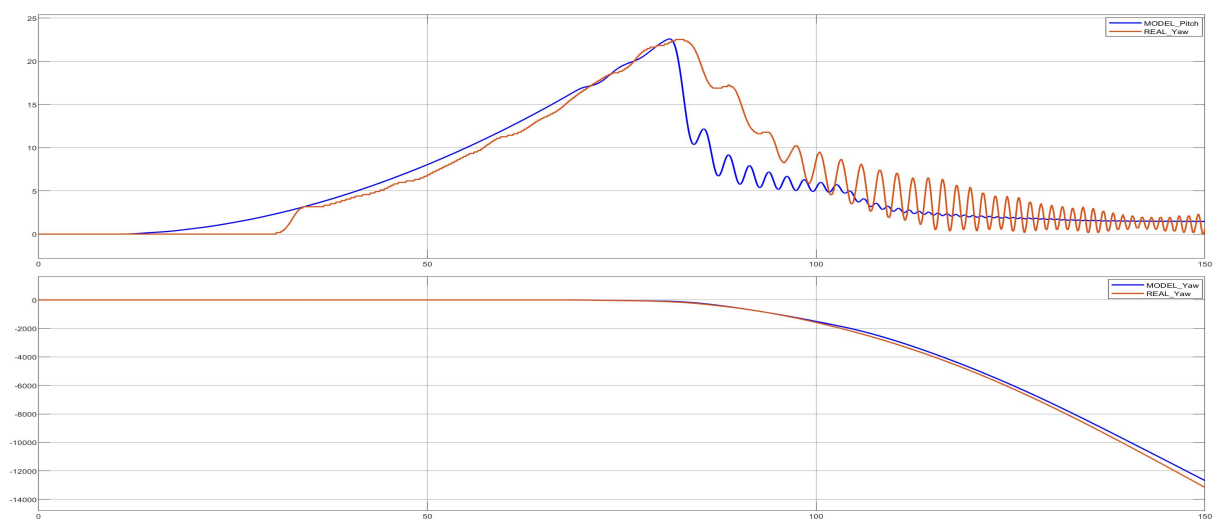


Figure 2.6: 2 DoF Model validation

2.2.2 Frequency Domain Validation

For the validation of Equation 1.12 we used the same strategy as in subsection 2.1.2, below are shown the Frequency Based Model Validation results:

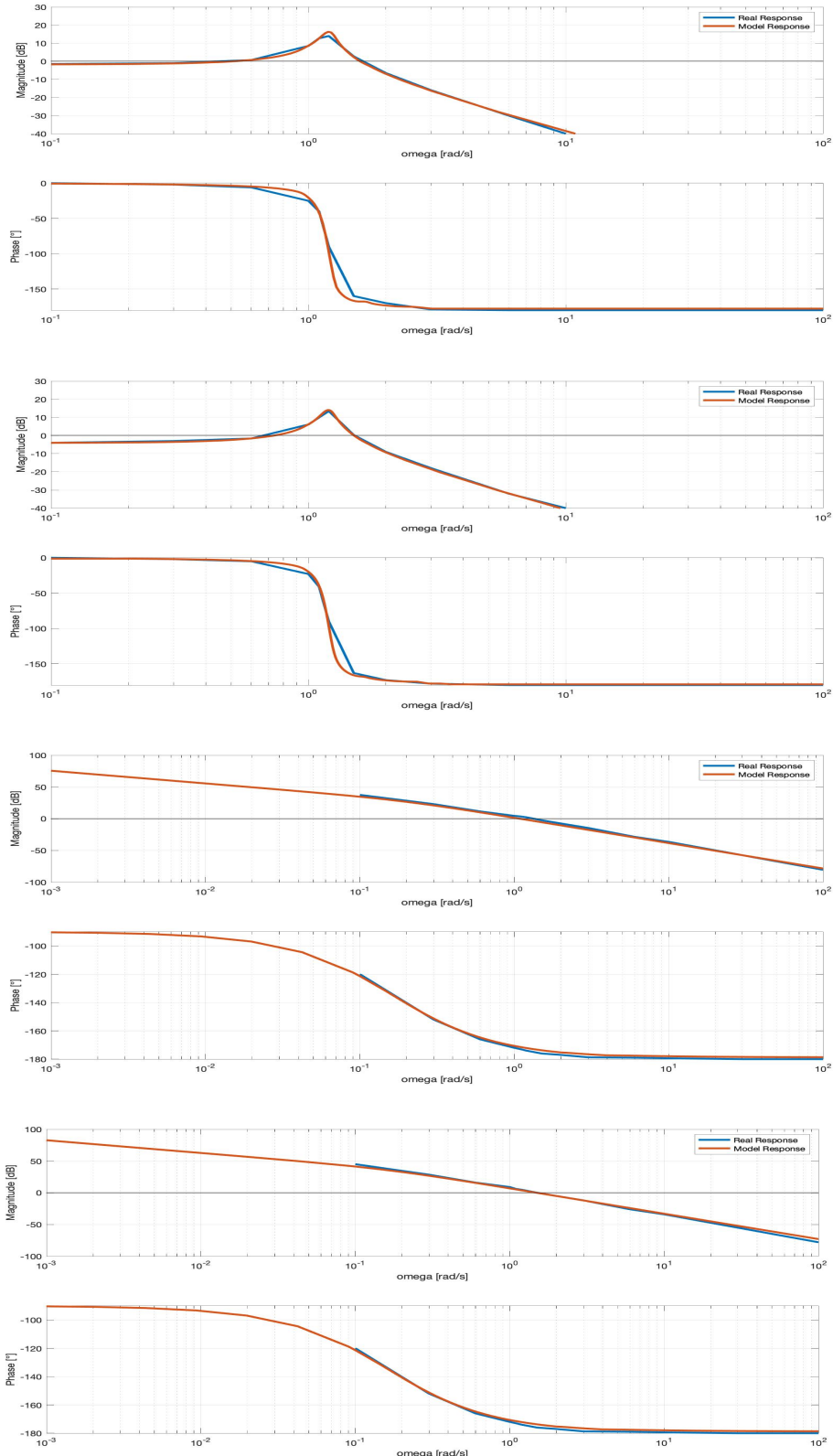


Figure 2.7: $G_{11}(s), G_{12}(s), G_{21}(s), G_{22}(s)$

Chapter 3

Control Design and Validation

3.1 1DoF Frequency Based Control

3.1.1 Synthesis

Desired Performances Given the system's Open-Loop Settling Time $T_s^{OL} = 45s$ we obtained the desired Closed-Loop settling time T_s as:

$$T_s = \frac{T_s^{OL}}{5} = 9s$$

Control Design For the Frequency Based Control objective, we designed a Reference Tracking Regulator on [Equation 1.1.1](#), the transfer function between the thrust forces (F_0 - F_1) and the Pitch Angle θ . In the first place, in order to obtain good static and dynamic performances, we decided to build a regulator with two complex conjugate zeros to cancel out the complex conjugate poles of $G(s)$, an integrator to have null asymptotic error, and a high frequency pole to preserve the phase margin of the loop transfer function.

Since the complex conjugate poles of the system are not fixed (see [Figure 1.4](#)) it was impossible to achieve an analytical cancellation, therefore we decided to slightly anticipate the regulator's conjugate zeros while increasing their damping factor to ensure a suitable cancellation. This choice led us to a more robust regulator.

Notice that before performing the cancellation we made sure, thanks to Routh criterion, that the poles had negative real part in order to avoid critical cancellations. Here is reported the designed regulator $R(s)$:

$$R(s) = \frac{s^2 + 2s\omega_{nr}\zeta + \omega_{nr}^2}{s(1 + 0.001s)} \quad \text{see } (\textcolor{blue}{A})$$

Performances In the following, the Open-Loop Transfer Function $L(s)$ ([Figure 3.1](#)) and the Closed-Loop Transfer Function $T(s)$ ([Figure 3.2](#)) of the controlled system will be analyzed.

We can observe through $L(s)$ that the designed regulator ensures the previously prescribed performances in terms of Settling Time and Phase Margin while preserving robustness, the final regulator provides a Settling Time $T_s = 8.7s$ with a Phase Margin $\varphi_m = 92.2^\circ$ and zero steady-state error due to the integral action.

Analyzing $T(s)$ it is possible to observe that, in the neighbourhood of the natural frequency ω_n , the attenuation (i.e.: Magnitude lower than 0dB) avoids potentially harmful resonance effects which, if amplified, would lead to oscillatory response.

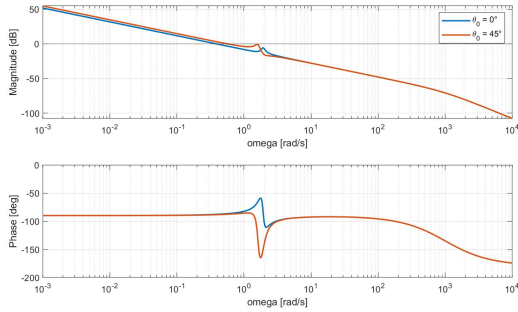


Figure 3.1: Open-Loop Transfer Function

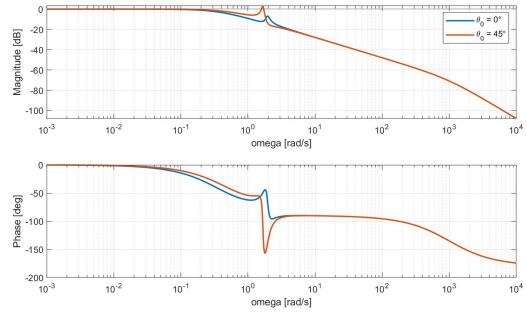


Figure 3.2: Closed-Loop Transfer Function

Baseline Design Since we modelled the Aerodynamic behaviour of the Thrusters, we knew that, being the Motor Map a third order polynomial, at lower supplied voltages there is a sort of backlash in the Force delivery which translates in a time delay. This means that in normal condition, starting with both Motors off, the control action would need to counteract this phenomenon.

In order to overcome this annoying effect, and by doing so fasten the control system, we decided to change the initial conditions and start the Motors with the same Thrust Force so that the setup stays still but it is way more responsive as the Motors are controlled in a more linear working region.

Control Scheme

The final control scheme is here depicted :

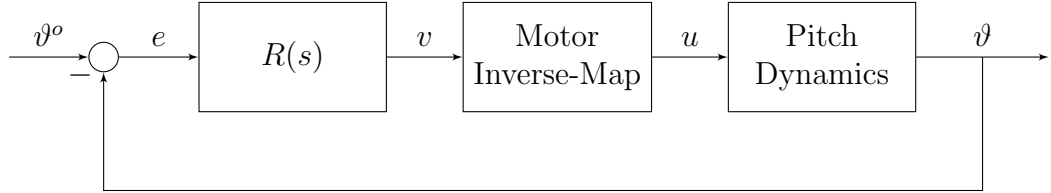


Figure 3.3: Frequency Based Pitch Control Scheme

3.1.2 Validation

Time Domain In Figure 3.4 the Reference Tracking of $R(s)$ in response to a multiple step signal is shown. It is possible to appreciate the baseline action at the start. Notice that the step starting in $t = 60s$ has a longer settling time as Motor 1 is changing its rotation direction therefore (as demonstrated in subsection 1.2.2) its thrust force is almost null for a while.

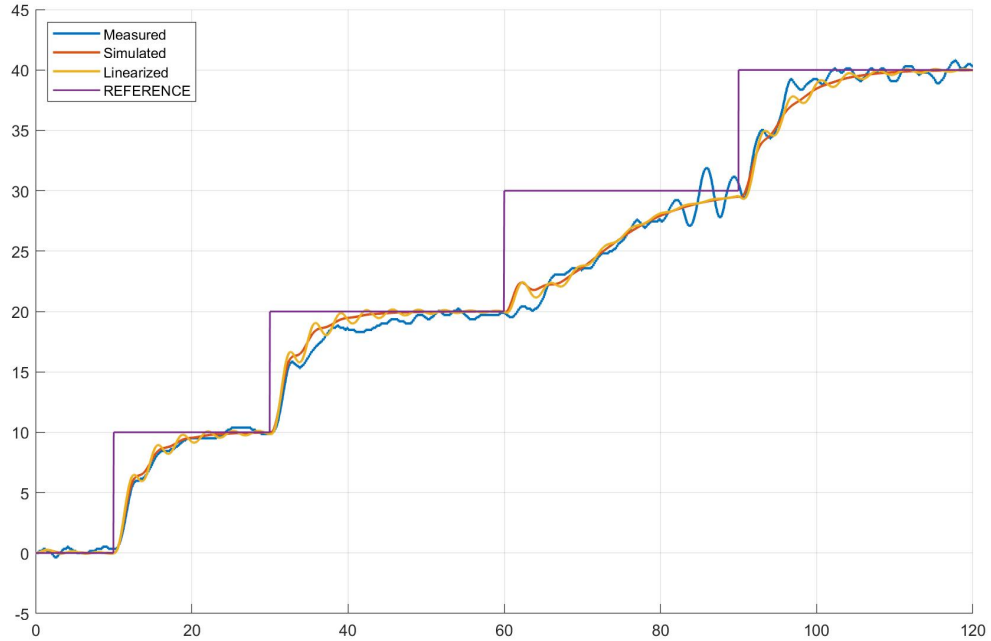


Figure 3.4: 1 DoF Reference Tracking Response

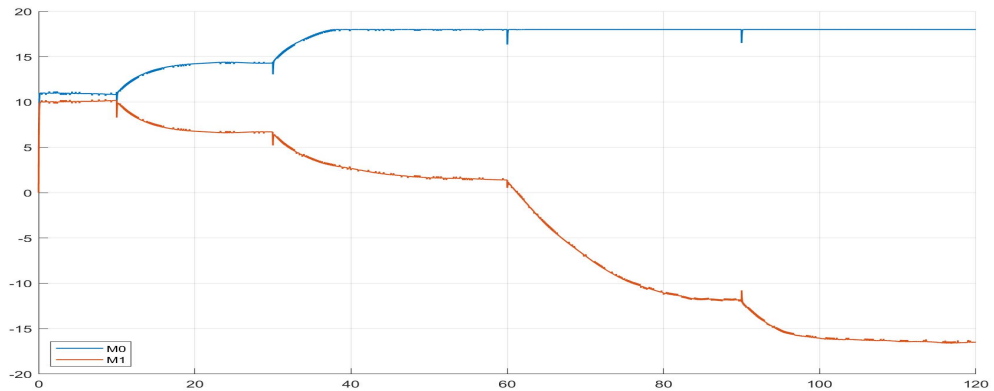


Figure 3.5: 1 DoF Reference Tracking Motor Actions

Frequency Domain With the same idea as in subsection 2.1.2 we validated the Closed-Loop Complementary Sensitivity Transfer Function for the controller and in Figure 3.6 it is shown the result.

In Figure 3.7 and in Figure 3.8 are shown, respectively, how the magnitude and phase shift were computed, note that this is just an example since these plots actually belong to the 1DoF Model Validation.

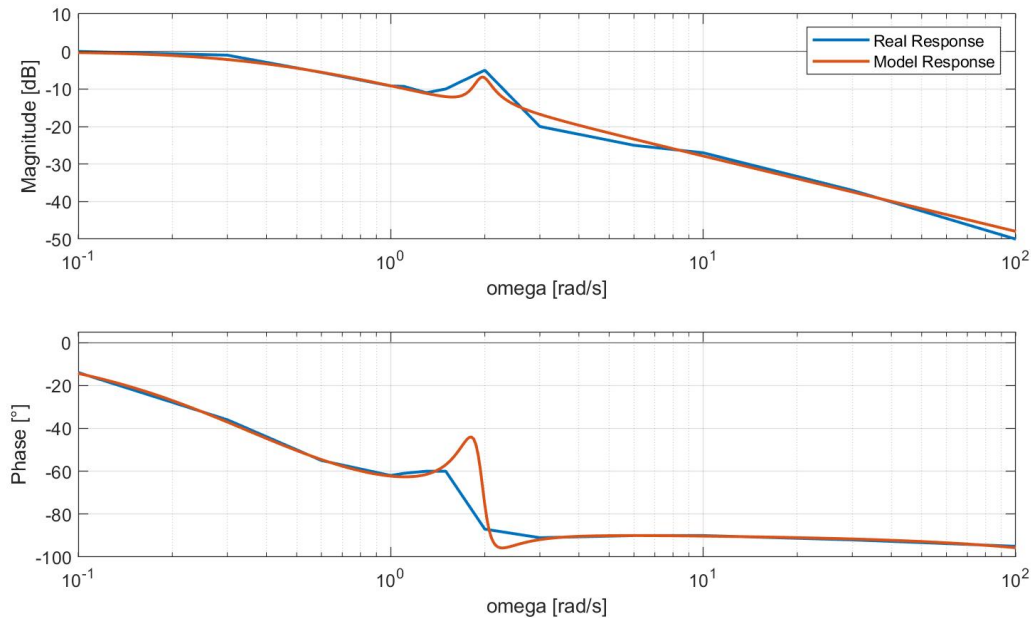


Figure 3.6: 1 DoF Complementary Sensitivity Function $T(s)$

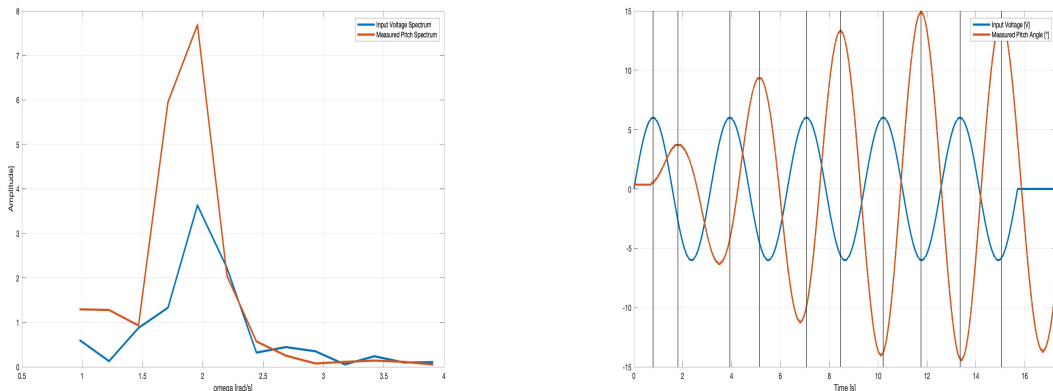


Figure 3.7: I/O FFT

Figure 3.8: I/O Phase Shift

3.2 2DoF Frequency Based Control

3.2.1 Synthesis

Inverted Decoupling Analyzing the 2 DoF Frequency Based model [Equation 1.12](#), being $G(s)$ non diagonal, it was clear that the system is coupled. Therefore our first goal was to develop a Inverted Decoupler to enable us to design two separate SISO controllers. Its scheme is represented in figure [Figure 3.9](#).

The decoupler $\Delta(s)$:

$$\Delta(s) = \begin{bmatrix} 0 & -\frac{G_{12}(s)}{G_{11}(s)} \\ -\frac{G_{21}(s)}{G_{22}(s)} & 0 \end{bmatrix} = \begin{bmatrix} 0 & -k_{yp} \\ -k_{py} & 0 \end{bmatrix} \quad (3.1)$$

pre-multiplies $G(s)$ and separates the two dynamics as follows:

$$G'(s) = G(s)\Delta(s) = \begin{bmatrix} G_{11}(s) & 0 \\ 0 & G_{22}(s) \end{bmatrix} \quad (3.2)$$

Notice that the found Decoupler is simply a Static one, the only possible drawback of this kind of scheme is that part of the control action is used to decouple, hence the Direct control can happen to be more sluggish.

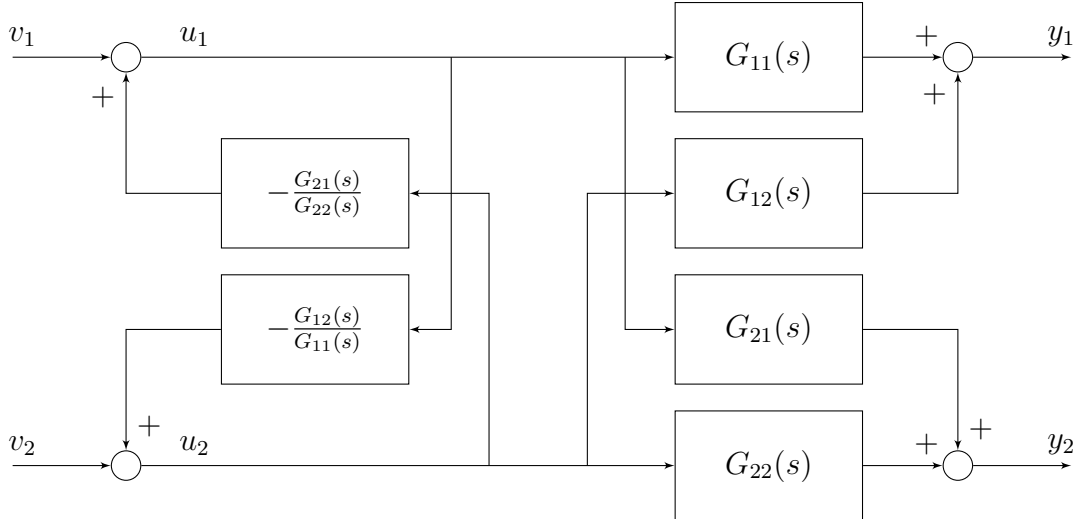


Figure 3.9: Inverted Decoupler Block Scheme

Desired Performances We defined the desired performances as explained in [subsection 3.1.1](#)

$$\begin{cases} T_{OL}^{pitch} = 35s \implies T_s^{pitch} = 7s \\ T_{OL}^{yaw} = 30s \implies T_s^{yaw} = 6s \end{cases}$$

Control Design For controller $R_1(s)$ we basically applied the same control strategy seen in [subsection 3.1.1](#) paying attention to the different Pitch Dynamics, due to the changed CoG position. As a result the designed controller was:

$$R_1(s) = \frac{s^2 + 2s\omega_{nr}\zeta + \omega_{nr}^2}{s(1 + 0.001s)} \quad \text{see } (A)$$

For controller $R_2(s)$, given G_{22} from [Equation 1.15](#), which we note being a transfer function with 2 poles only and no zeros, the regulator can be simply designed as a transfer

function with 2 zeros that perfectly cancel the system's poles and two poles, one being a pure integrator, which guarantees zero error at steady state, and the latter being a high frequency pole, guaranteeing first of all the causality of the regulator and secondly an high phase margin of the open-loop transfer function. We also added a gain in order to adjust the cutoff frequency. Trying to improve the performances we put an additional low frequency zero with another pure integrator since we saw that this choice particularly improved the performances, especially increasing the phase margin and consequently reducing the settling time.

As a result the controller transfer function is the following:

$$R_2(s) = \frac{0.9(s + 0.5)((J_y \cos^2 \theta_0 + M_b D_{m2}^2 \sin^2 \theta_0)s^2 + k_{yaw}s)}{s^2(1 + 0.001s)} \quad \text{see(A)}$$

Performances The first controller $R_1(s)$ has settling time $T_s^{pitch} = 10s$ and phase margin $\varphi_m^{pitch} = 79.1^\circ$ while $R_2(s)$ settles in $T_s^{yaw} = 9s$ with $\varphi_m^{yaw} = 76.4^\circ$.

The two designed regulators, despite being well robust, did not achieve the performances we prescribed in the first place in terms of Settling Time, for this reason we decided to Fine Tune two PID controllers as follows:

$$\begin{aligned} R_1^{PID}(s) &= 5 + \frac{1}{s} + \frac{3s}{(1 + 0.001s)} \\ R_2^{PID}(s) &= 1 + \frac{0.1}{s} + \frac{1.25s}{(1 + 0.001s)} \end{aligned}$$

These new controllers guarantee a settling time $T_s = 4s$ while preserving the phase margin. In the following, their Open-Loop Transfer Functions $L_{11}(s)$ and $L_{22}(s)$ and their Complementary Sensitivity Functions $T_{11}(s)$ and $T_{22}(s)$ are shown.

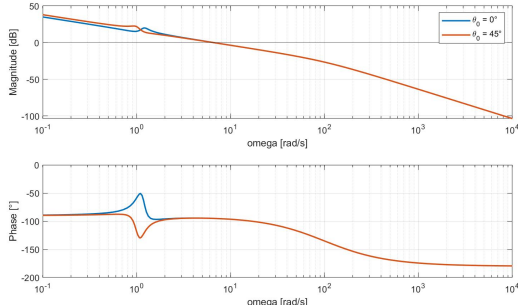


Figure 3.10: $L_{11}(s)$

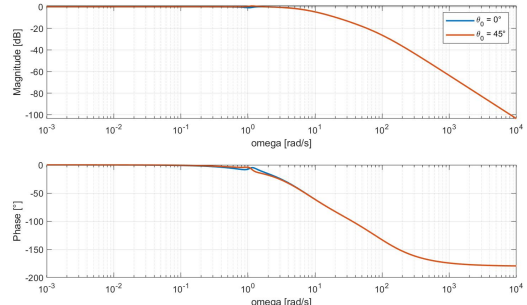


Figure 3.11: $T_{11}(s)$

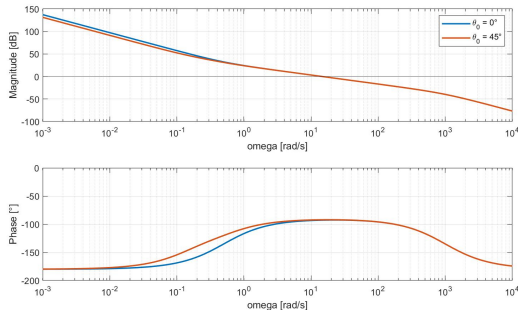


Figure 3.12: $L_{22}(s)$

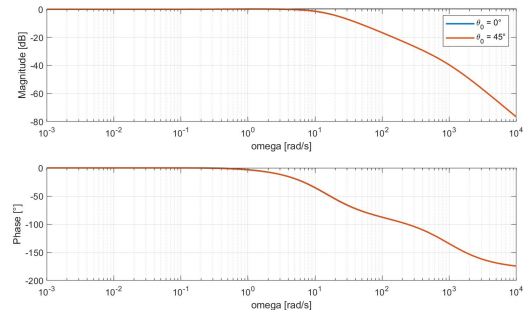


Figure 3.13: $T_{22}(s)$

Anti Wind-Up Configuration

For the Yaw Dynamics, since we noticed very huge overshoots, it became necessary to put the regulator $R_2(s)$ in Anti Wind-up Configuration. This particular scheme avoids the integral wind-up effects when the Motor needs to change its thrust force direction and led us to a solution without any overshoot. In the Pitch this wasn't necessary since it is less common a control variable saturation and also because the CoG acts as a "natural anti wind-up".

Control Scheme

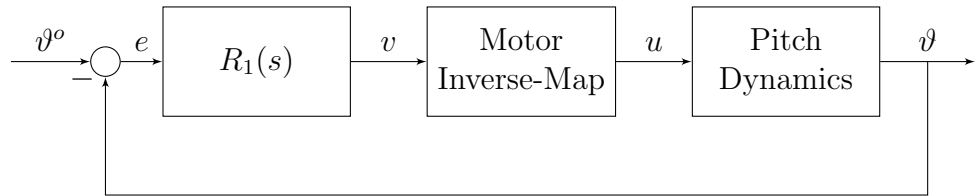


Figure 3.14: Frequency Based Pitch Control Scheme

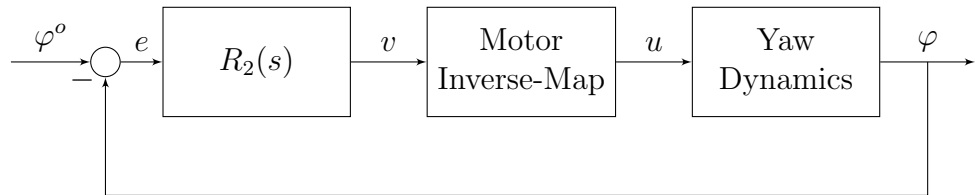


Figure 3.15: Frequency Based Yaw Control Scheme

3.2.2 Validation

Time Domain Here the controllers are validated in Reference Tracking, in Figure 3.16 it is shown the Pitch and Yaw Response to simultaneous steps in both angles.

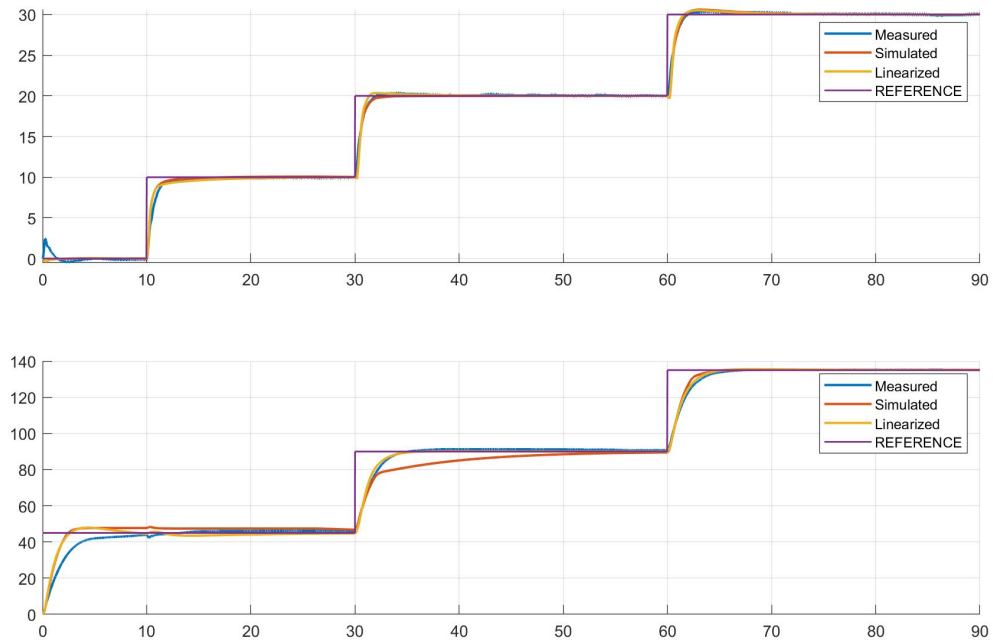


Figure 3.16: 2 DoF Anti Wind-Up Validation in TD

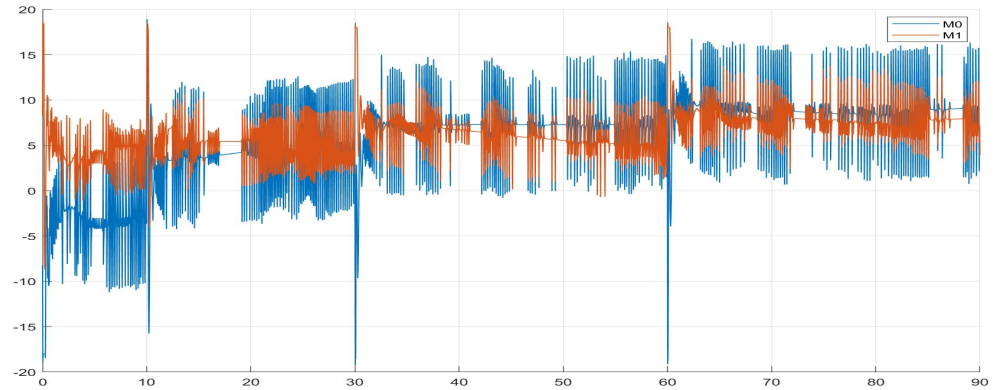


Figure 3.17: 2 DoF Anti Wind-Up Motors

Frequency Domain With the same pseudo sine-sweep experiment as in subsection 2.1.2, now supplying the setup reference angles instead of voltages, we computed the following Complementary Sensitivity Functions which clearly validate the controller in Frequency Domain.

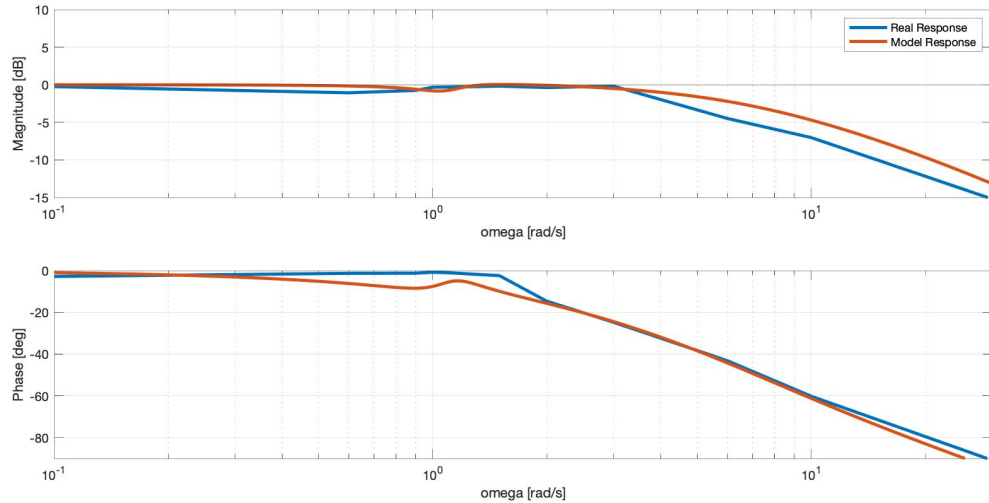


Figure 3.18: Pitch Complementary Sensitivity $T_{11}(s)$

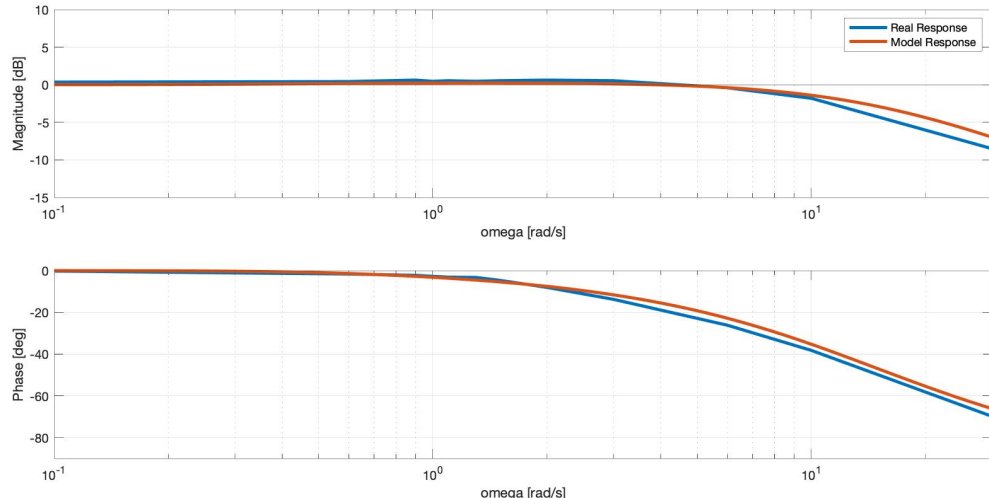


Figure 3.19: Yaw Complementary Sensitivity $T_{22}(s)$

3.3 Pole Placement with State Observer

3.3.1 Synthesis

In the following, it is discussed the use of State-Space Control Techniques for Reference Tracking starting from our State-Space Model shown in [Equation 1.9](#).

The objective will be to compute a State-Feedback Control Law in the form:

$$u(t) = -Kx(t) + v(t) \quad (3.3)$$

where $v(t)$ is used for external control loops. From now on, it will be considered null as there is no external loop in our design. Since not all the state variables are measurable it was necessary to design State Observers to estimate the non-measurable states.

Pole Placement Pole Placement allows to compute a Gain Matrix K for the Control Law that imposes prescribed Closed-Loop poles to the system, indeed the Closed-Loop system with $u(t)$ as described above becomes (under the assumption that the pair (A, B) is reachable):

$$\dot{x} = (A - BK)x \quad (3.4)$$

therefore the Closed-Loop Poles will be the eigenvalues of the matrix $(A - BK)$. For our control objective we actually designed the Pole Placement on the Enlarged System derived in [Equation 1.1.2](#), this system includes the tracking error, therefore the project on the Enlarged System allowed us to achieve a zero steady-state error.

Luenberger State Observer The State Observer allows to estimate the states of a system as a function of its Input variable and its Measurable Outputs (under the assumption that the pair (A, C) is observable) as follows:

$$\dot{\hat{x}} = A\hat{x} + Bu + L(y - \hat{y}) \quad (3.5)$$

which results in:

$$\dot{\hat{x}} = (A - LC)\hat{x} + Bu + Ly$$

Note that the eigenvalues of $(A - LC)$ are the State Observer's poles.

Control Design From the *separation principle* we know that the Closed-Loop poles of the system subject to Pole Placement and State Observer are the ones of $(A - BK)$ and $(A - LC)$ therefore we imposed the Closed-Loop Poles of the Regulator to be in the neighbourhood of $\omega = 1.2\text{rad/s}$ by means of Fine Tuning as we noticed that higher bandwidth led to instability while lower ones reduced the system's responsiveness.

As for the State Observer it was designed to be at least a decade faster than the Pole Placement, hence its Poles are in the neighbourhood of $\omega = 120\text{rad/s}$. Once completed the design the matrix K and L were computed with the MatLab® *place* command.

Control Scheme

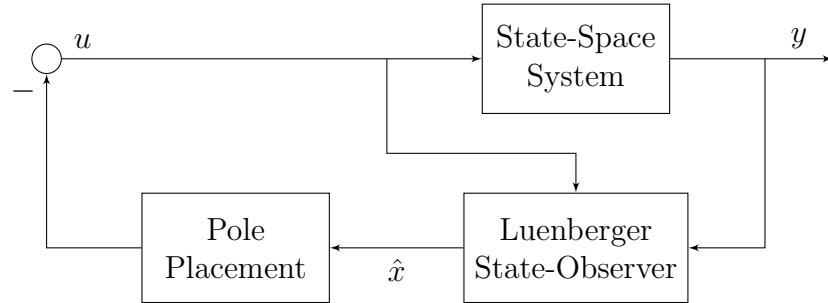


Figure 3.20: Pole Placement with Luenberger State Observer Control Scheme

3.3.2 Validation

Time Domain In Figure 3.21 it is shown the Pole Placement response to a step signal for the Reference Tracking Objective.

It is clearly observable an oscillation for small angles (which appears only on the setup) while for higher references it becomes very precise. We attributed this effect to the lack of a time delay in our Motor Maps model, this is definitely not negligible at low voltages and leads to this unpleasant response.

Unfortunately we did not have time to fix this problem.

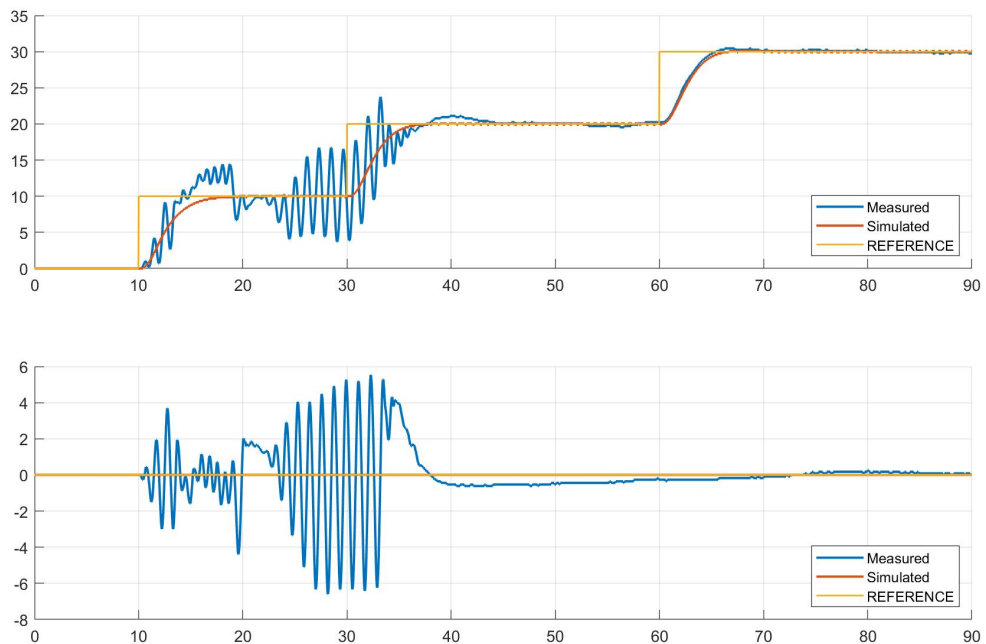


Figure 3.21: Pole Placement Reference Tracking Response

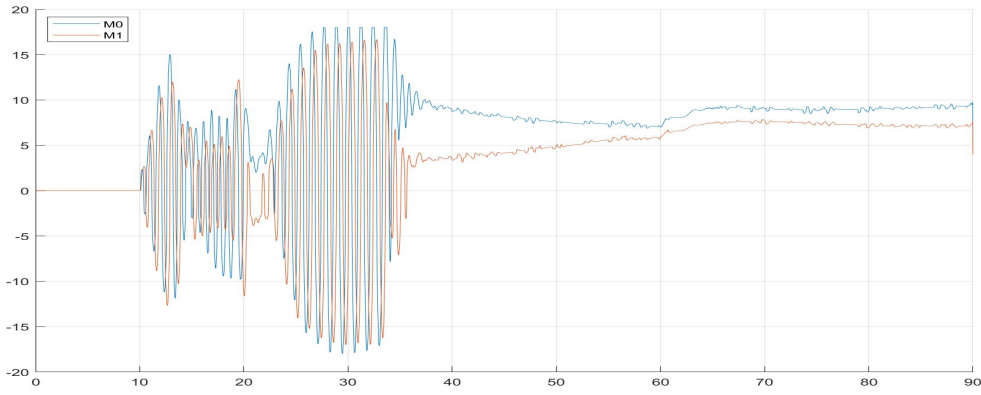


Figure 3.22: Pole Placement Reference Tracking Motor Actions

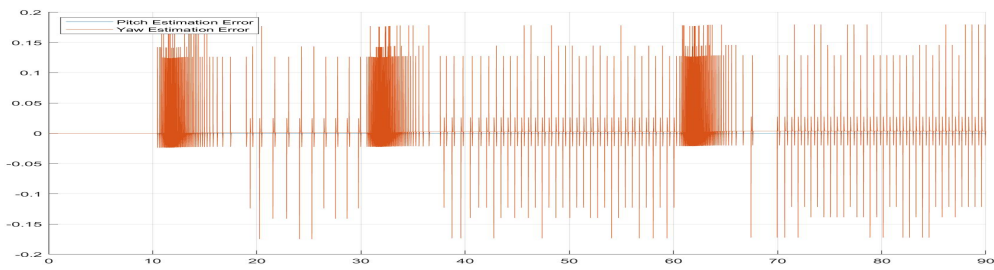


Figure 3.23: State Observer Estimation Errors

[Figure 3.24](#) shows the Attitude Tracking Response of the Pole Placement highlighting the same flaws described before.

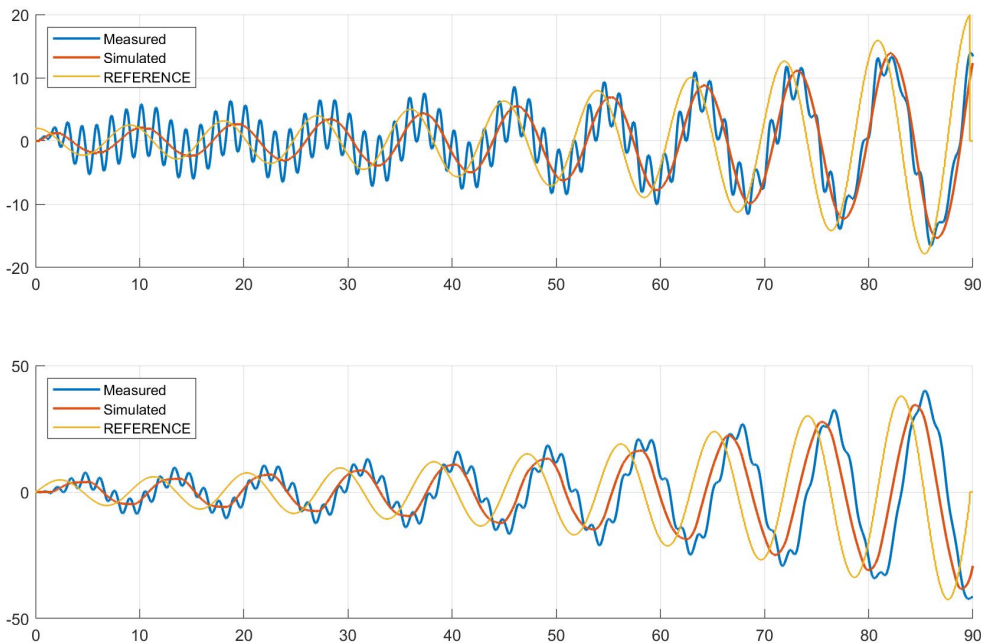


Figure 3.24: Pole Placement Attitude Tracking Response

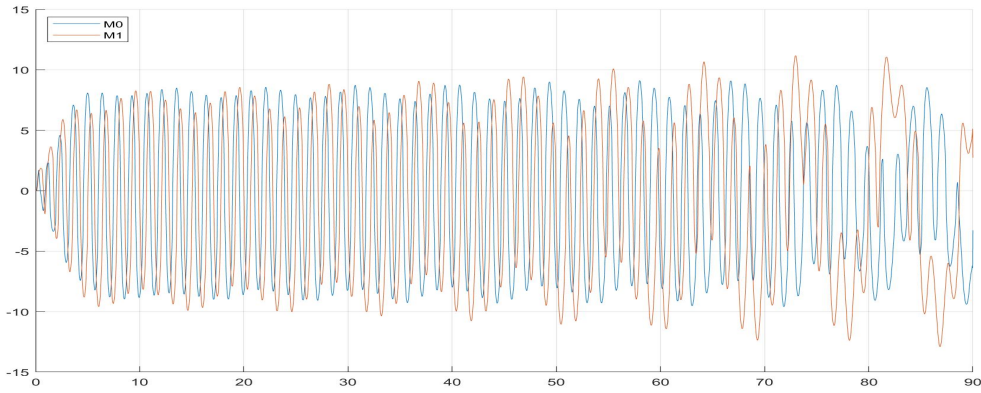


Figure 3.25: Pole Placement Attitude Tracking Motor Actions

Frequency Domain Sad to say, we did not manage to complete the sine-sweep experiment for this controller. The only thing we can do to try an heuristic (non)validation is to underline that in [Figure 3.24](#) it is possible to see that the real Sensitivity Function must have higher bandwidth than the desired one since we observe the high frequency oscillations superimposed to the actual signal in the output.

3.4 LQG Control

3.4.1 Synthesis

This control strategy combines the LQ solution to a deterministic problem and a Kalman filter used for the state estimation when stochastic noises affect the process. Consider the state space system in [section 1.1.2](#) where also noises are considered. The overall regulator is described by:

$$\begin{cases} \dot{\hat{x}}(t) = A\hat{x}(t) + Bu(t) + \bar{L}(y(t) - C\hat{x}(t)) \\ u(t) = -\bar{K}\hat{x}(t) \end{cases} \quad (3.6)$$

LQ Control This type of control strategy seeks to find an optimal control action by minimizing a quadratic cost function that keeps in count the weighted control action and state. This works under the assumption that (A, B) is Observable and (A, C_q) ($C_q = \sqrt{Q}$) is Reachable.

$$J = \int_0^T (x'(\tau)Qx(\tau) + u'(\tau)Ru(\tau)) d\tau \quad (3.7)$$

The weights Q and R are our design choice

We solved the infinite horizon control problem in which $T \rightarrow \infty$ by using the [Differential Riccati Equation](#) trough *lqr* MatLab® command.

In order to tune Q and R parameters we first started with the Bryson's rule in which the two matrices are diagonal with:

$$Q_{ii} = \frac{1}{\max(x_i)^2} \quad \text{and} \quad R_{ii} = \rho \frac{1}{\max(u_i)^2} \quad \text{see (A)}$$

Then slight modifications were made to guarantee better results than the theoretical ones.

Kalman Predictor In order to obtain the full state vector, we used a state observer since the measurements of the two velocities weren't available.

The Kalman Filter is applicable if observability of (A, C) and reachability of (A, B_q) ($B_q = \sqrt{\tilde{Q}}$) are fulfilled. The observer used in this strategy is a steady state Kalman Filter, where \tilde{L} is defined as follow:

$$\tilde{L} = \tilde{P}C'\tilde{R}^{-1} \quad \text{where} \quad 0 = A\tilde{P} + \tilde{P}A' + \tilde{Q} - \tilde{P}C'\tilde{R}^{-1}C\tilde{P}$$

Notice that Q and R are LQ's parameters while \tilde{Q} and \tilde{R} are KF's parameters.

In order to find the correct parameters \tilde{Q} and \tilde{R} the *Loop Transfer Recovery* method was used:

$$\tilde{Q} = \alpha(BB') \quad \text{and} \quad \tilde{R} = I, \quad \text{see (A)}$$

With $\alpha \rightarrow \infty$ leads to the LTR result. In short words, the Loop transfer function tends to the ideal and desired Loop transfer function.

Control Scheme

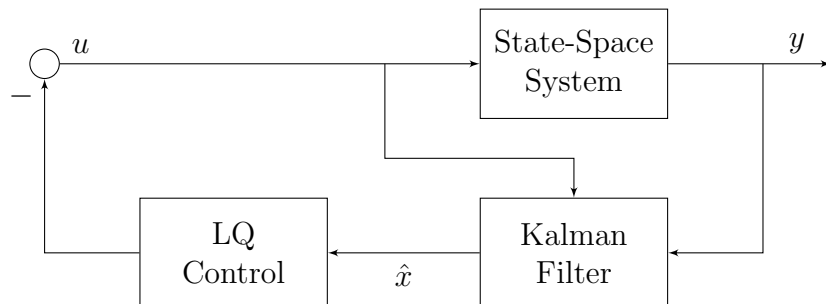


Figure 3.26: LQG Control Scheme

3.4.2 Validation

Time Domain In Figure 3.27 it is shown the LQG response to a multiple steps Reference Tracking, this clearly validates the controller in Time Domain.

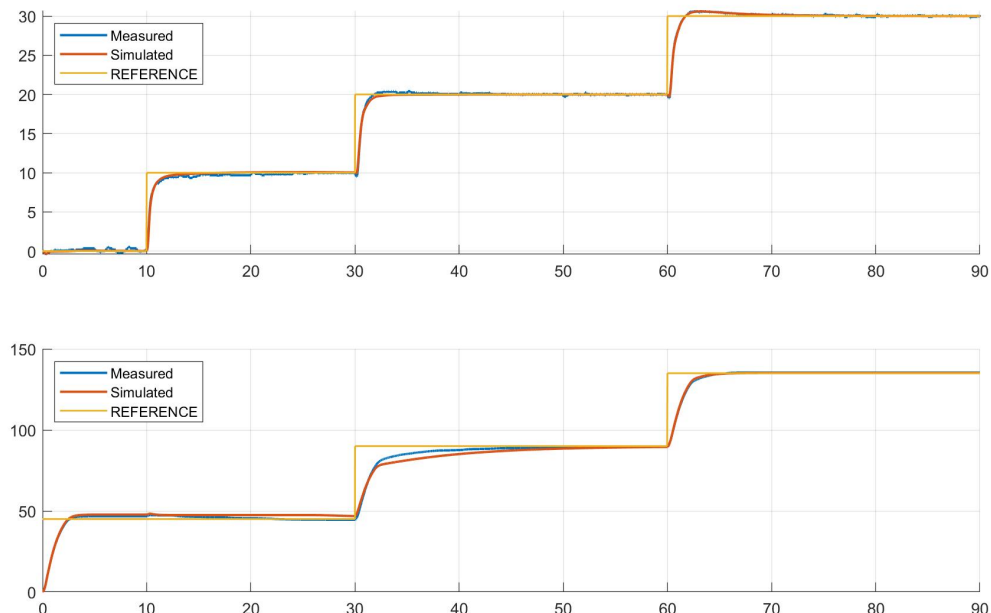


Figure 3.27: LQG Reference Tracking Response

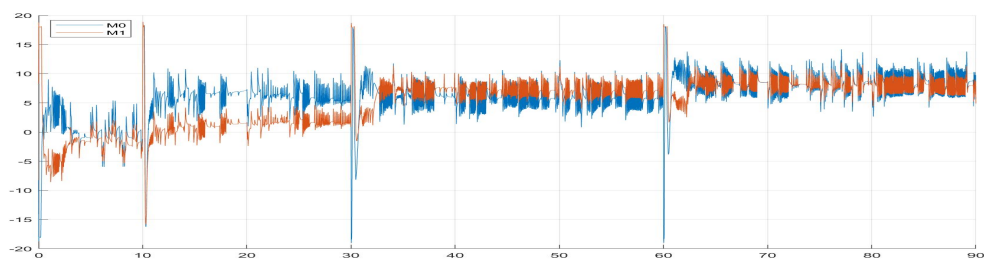
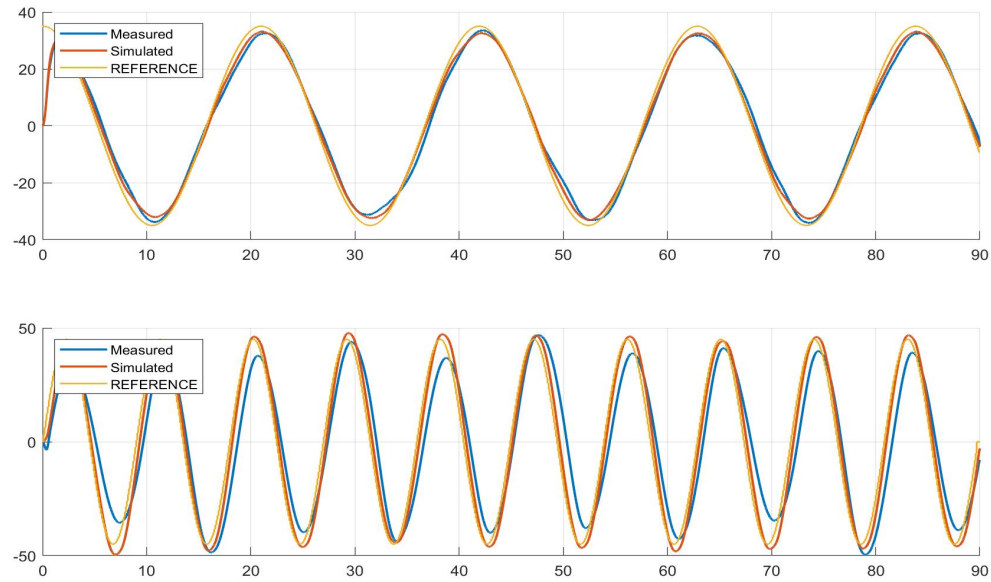
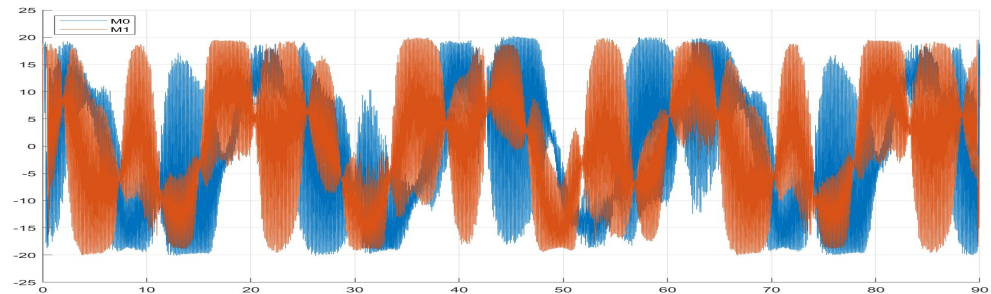


Figure 3.28: LQG Reference Tracking Motor Actions

The Attitude Tracking results are displayed in [Figure 3.29](#), in this case the result was almost perfect confirming the controller validation.



[Figure 3.29: LQG Attitude Tracking](#)



[Figure 3.30: LQG Attitude Tracking Motors](#)

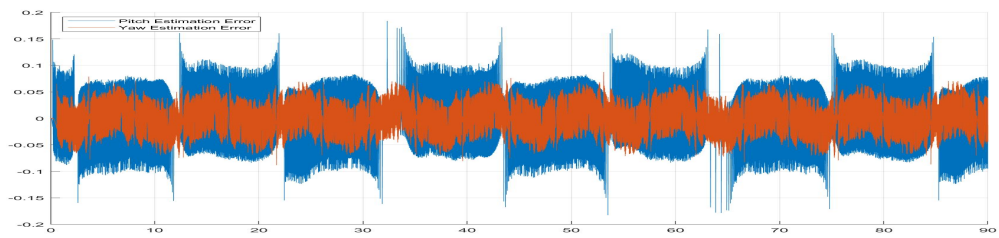


[Figure 3.31: LQG Attitude Tracking Kalman Filter Prediction Error](#)

Frequency Domain As for the Pole Placement there was no time to complete this task. What we can say is that from [Figure 3.29](#) analysis we can infer that, at least at the experiment frequencies, the Bode Plot would have been coherent since the tracking is almost perfect.

3.5 Model Predictive Control

3.5.1 Synthesis

This advanced control technique has many different variants, we decided to implement a Linear Model Predictive Control with [Equation 1.9](#) as Process Internal Model. The original control problem was reformulated into an optimization one where the optimal control action is obtained by minimizing a cost function, that depends on the state and the control action itself, through a future simulation on its internal model over a Prediction Horizon N.

The cost function is the following:

$$J(x(k), u(.), k) = \sum_{i=0}^{N-1} [x(k+i)'Qx(k+i) + u(k+i)'Ru(k+i)] + x(k+N)'Sx(k+N) \quad (3.8)$$

where Q, R, S and N are the actual design choices being the optimization weights and the Prediction Horizon. Moreover MPC allows to solve the optimization problem subject to constraints, such as saturation on Inputs and Outputs. Finally it is also possible to define a Control Horizon $N_u < N$ in order to lighten the computation, in this case the MPC optimizes the first N_u optimal control variables and imposes the other ones equal to $u[k + N_u]$, in the following a clue on our design choices.

Sampling Time Given a minimum desired Closed-Loop settling time T_s^{min} the Sampling Time T_{sample} is commonly chosen as $T_{sample} = (0.1 \div 0.25)T_s^{min}$. We supposed $T_s^{min} = 3s$ and, consequently, chose $T_{sample} = 0.6s$.

Prediction Horizon It is good a practice to choose the Prediction Horizon such that $15 < N < 50$, we chose $N = 50$ so that $T_{sample}N = T_s^{min}$. Since this choice could lead to heavy computation we defined a Control Horizon $N_u = 4$.

Constraints We specified the following constraints on the Input variables to take into account the Motors saturation:

$$u_0[k] = F_0 \in [F_0^{min}, F_0^{max}] \quad u_1[k] = F_1 \in [F_1^{min}, F_1^{max}]$$

and this on the state related to the Pitch Motion and describing the the angle bottoming:

$$x_1[k] = \theta[k] \in [\theta_{min}, \theta_{max}]$$

Q and R Matrices - A Fine Tuning Approach Since there isn't an algorithmic way to compute Q and R matrices, to assign their values, we used our common sense in what is called Fine Tuning (or "a manina" approach).

Control Scheme

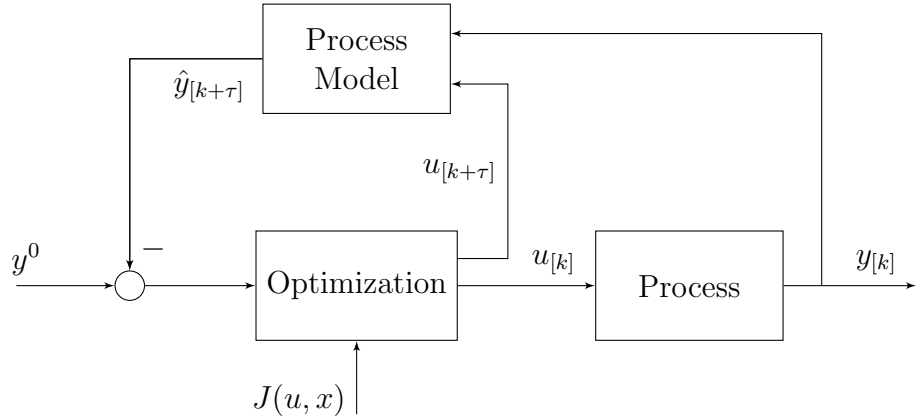


Figure 3.32: Model Predictive Control Block Scheme

3.5.2 Validation

Time Domain In Figure 3.33 it shown the response of the designed MPC to the Attitude Tracking Control Objective. While not being perfect it almost follows correctly the Reference Signal with some unwanted high frequencies components.

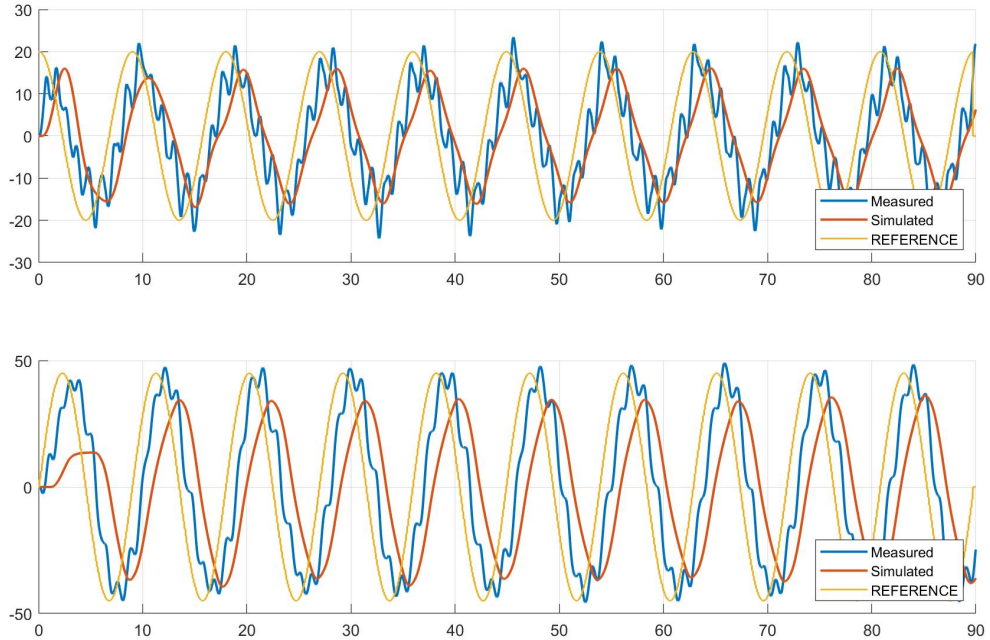


Figure 3.33: MPC Attitude Tracking Response

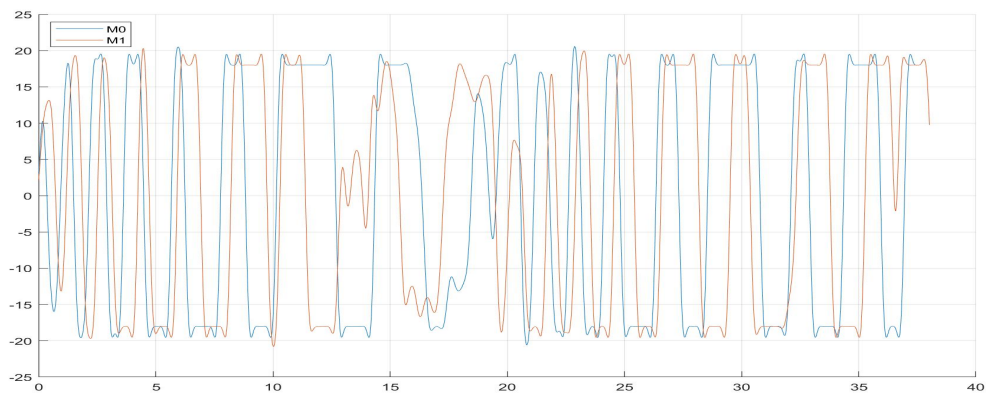


Figure 3.34: MPC Attitude Tracking Motor Actions

Appendix A

Explicit Results

1 DoF Regulator

$$R(s) = \frac{0.055s^2 + 0.0312s + 0.1965}{0.001s^2 + s}$$

2 DoF Decoupled

$$R_{11}(s) = \frac{0.36s^2 + 0.1346s + 0.4356}{0.001s^2 + s} \quad R_{22}(s) = \frac{0.9s^2 + 0.598s + 0.07398}{0.001s^2 + s}$$

PP Results

$$\text{ClosedLoop_poles} = -[1.05, 1.06, 1.07, 1.08, 1.09, 1.10] \quad \text{Observer_poles} = -[120, 113, 100, 107]$$

$$L = 10^3 \times \begin{bmatrix} 0.022 & 0.005 \\ 1.149 & 0.055 \\ 0.001 & 0.023 \\ 0.054 & 1.258 \end{bmatrix} \quad K = \begin{bmatrix} 1.15 & 0.57 & -1.09 & -0.49 & -0.92 & 0.78 \\ 0.79 & 0.36 & 1.38 & 0.63 & -0.57 & -0.99 \end{bmatrix}$$

LQG Results

$$Q = 10^5 \times \begin{bmatrix} 32.3 & 0 & 0 & 0 & 0 & 0 \\ 0 & 0.7 & 0 & 0 & 0 & 0 \\ 0 & 0 & 129.1 & 0 & 0 & 0 \\ 0 & 0 & 0 & 1 & 0 & 0 \\ 0 & 0 & 0 & 0 & 100 & 0 \\ 0 & 0 & 0 & 0 & 0 & 204.1 \end{bmatrix} \quad R = \begin{bmatrix} 1 & 0 \\ 0 & 1.44 \end{bmatrix} \quad \rho = 100$$

$$\bar{K} = \begin{bmatrix} 0.52 & 0.29 & -0.73 & -0.33 & -0.51 & 0.53 \\ 0.31 & 0.18 & 0.86 & 0.40 & -0.31 & -0.61 \end{bmatrix}$$

$$\tilde{Q} = 10^5 \times \begin{bmatrix} 0 & 0 & 0 & 0 \\ 0 & 8.7 & 0 & 0.7 \\ 0 & 0 & 0 & 0 \\ 0 & 0.7 & 0 & 6.3 \end{bmatrix} \quad \tilde{R} = \begin{bmatrix} 1 & 0 \\ 0 & 1 \end{bmatrix} \quad \alpha = 10000$$

$$\bar{L} = \begin{bmatrix} 42.95 & 0.97 \\ 923.00 & 40.18 \\ 0.97 & 39.56 \\ 40.19 & 783.33 \end{bmatrix}$$

MPC Results Final used weights for the linear MPC design:

$$MV = [1.4, 2.5] \quad MVRate = [22.5, 18.75] \quad OV = [2.25, 3.5]$$

Where MV are Manipulated Variables, MVRate are the Manipulated Variables Rates, OV are the Output Variables

Appendix B

Used Simulink Control Schemes

1 DoF [Helicopter_Template1DoF.slx](#)

Baseline partition [Baseline_Partition.slx](#)

2 DoF Decoupled [Helicopter_Template2DoF_Decoupled.slx](#)

Decoupler [Decoupler.slx](#)

2 DoF Anti-WindUp [Helicopter_Template2DoF_Anti_Windup.slx](#)

Pole Placement control [Helicopter_Template_PP.slx](#)

Linear Quadratic Gaussian control [Helicopter_Template_LQG.slx](#)

Model Predictive Control [Helicopter_Template_MPC.slx](#)

Bibliography

- [AS21] Elkhatem Aisha and Engin Seref. Robust lqr and lqr-pi control strategies based on adaptive weighting matrix selection for a uav position and attitude tracking control. *University*, 2021.
- [BT15] Paolo Bolzern and Mara Tanelli. *Fondamenti di controlli automatici*. Mc Graw Hill education, 2015.
- [Chr24] Xenophontos Christos. A beginner's guide to matlab. *Loyola College*, 2024.
- [Dav13] Di Ruscio David. Model predictive control with integral action: a simple mpc solution. *Telemark University College*, 2013.
- [F.19] Previdi F. Schemi di controllo avanzati, 2019.
- [Mat23a] MatLab. Choose sample time and horizons, 2023.
- [Mat23b] MatLab. Lowpass-filter signals, 2023.
- [Mot23] Allied Motion. Cl40 (7w) specifications. *Allied Motion*, 2023.
- [QI11] Innovative Education QUANSER Inc. Matlab/simulink and quarc primer. *Quanser Inc.*, 2011.
- [QI16] Innovative Education QUANSER Inc. User manual quanser aero set up and configuration. *Quanser Inc.*, 2016.
- [R.06] Murray R. Lecture 2 - lqr control. *University*, 2006.
- [SJ21] Schlanbusch Siri and Zhou Jing. Adaptive backstepping control of a 2-dof helicopter. *University*, 2021.
- [SM20] Riccardo Scattolini and Lalo Magni. *Advanced and Multivariable Control*. Pitagora Editrice Bologna, 2020.
- [Ste22a] Bruni Stefano. Lesson 1. *Politecnico di Milano*, 2022.
- [Ste22b] Bruni Stefano. Lesson 2. *Politecnico di Milano*, 2022.
- [Ste22c] Bruni Stefano. Lesson 4. *Politecnico di Milano*, 2022.
- [Tut18] TutorialsPoint.com. Response of the first order system, 2018.
- [VISC18] S.Bhat Vinayambika, Thirunavukkarasu I., Shanmuga Priya S., and Shreesha C. Predictive control algorithm based on integral action- design and implementation. *Mangalore University*, 2018.
- [Vos17] Chris Voss. *Never Split the Difference*. Harper USA, 2017.
- [Z.20] Azizah Z. Inverted decoupling mimo internal model control using mp tuning, 2020.